

A 10 μ m spectroscopic survey of Herbig Ae star disks: grain growth and crystallization*

R. van Boekel^{1,2}, M. Min¹, L.B.F.M. Waters^{1,3}, A. de Koter¹, C. Dominik¹,
M.E. van den Ancker², and J. Bouwman⁴

¹ Astronomical Institute “Anton Pannekoek”, University of Amsterdam,
Kruislaan 403, NL-1098 SJ Amsterdam, The Netherlands

² European Southern Observatory, Karl-Schwarzschildstrasse 2, D-85748
Garching bei München, Germany

³ Instituut voor Sterrenkunde, Katholieke Universiteit Leuven, Celestijnenlaan
200B, B-3001 Heverlee, Belgium

⁴ Max-Planck-Institut für Astronomie, Königstuhl 17, 69117 Heidelberg,
Germany

Received 2004 November 9; accepted 2005 March 4

Abstract. We present spectroscopic observations of a large sample of Herbig Ae stars in the 10 μ m spectral region. We perform compositional fits of the spectra based on properties of homogeneous as well as inhomogeneous spherical particles, and derive the mineralogy and typical grain sizes of the dust responsible for the 10 μ m emission. Several trends are reported that can constrain theoretical models of dust processing in these systems: *i*) none of the sources consists of fully pristine dust comparable to that found in the interstellar medium, *ii*) all sources with a high fraction of crystalline silicates are dominated by large grains, *iii*) the disks around more massive stars ($M \gtrsim 2.5 M_{\odot}$, $L \gtrsim 60 L_{\odot}$) have a higher fraction of crystalline silicates than those around lower mass stars, *iv*) in the subset of lower mass stars ($M \lesssim 2.5 M_{\odot}$) there is no correlation between stellar parameters and the derived crystallinity of the dust. The correlation between the shape and strength of the 10 micron silicate feature reported by van Boekel et al. (2003) is reconfirmed with this larger sample. The evidence presented in this paper is combined with that of other studies to present a likely scenario of dust processing in Herbig Ae systems. We conclude that the present data favour a scenario in which the crystalline silicates are produced in the innermost regions of the disk, close to the star, and transported outward to the regions where they can be detected by means of 10 micron spectroscopy. Additionally, we conclude that the final crystallinity of these disks is reached very soon after active accretion has stopped.

Key words. Stars: circumstellar matter: pre-main-sequence stars - Infrared: ISM: lines and bands

1. Introduction

A characteristic shared by many young, low and intermediate mass stars is the presence of a strong infrared excess. This radiation emerges from circumstellar dust grains left over from the star formation process. The material is believed to reside in a disk which is formed as a result of angular momentum conservation in the collapsing molecular cloud. After an initial strong accretion phase, a much longer pre-main-sequence phase ensues during which the disk slowly dissipates, and possibly planets are formed.

The interstellar dust which finds its way into a proto-planetary disk will undergo large changes in average size and chemical composition. These changes trace the process of disk dissipation and planet formation. Our solar system contains a precious record of the processes that took place during its formation. Comparison of this record to what is observed around young pre-main-sequence stars provides important insight into the history of our own solar system, and helps to constrain planet formation models.

The infrared spectral region is rich in vibrational resonances of abundant dust species. Therefore, infrared spectroscopy can be used to determine the composition of dust in proto-planetary disks, as well as constrain the size and shape of the dust grains. Analysis of the infrared (IR) dust emission features originating from the disk surface layer can be used to establish to what extent the dust composition in the disk has evolved away from that seen in the interstellar medium (ISM). For instance, crystalline silicates appear absent in the ISM (e.g. Demyk et al. 2000; Kemper et al. 2004) but are a substantial component in (some) comets and in interplanetary dust particles (MacKinnon & Rietmeijer 1987; Bradley et al. 1992). Clearly, the refractory material in the proto-solar cloud went through large changes as the solar system was formed. It should be kept in mind that spectroscopy in the 10 micron region is sensitive to a limited grain size range: large grains (with sizes above a few μm , depending on chemical composition and wavelength) show only weak spectral structure and do not contribute significantly to the infrared emission features.

In this work we study the composition of dust in the circumstellar environment of Herbig Ae/Be stars (Herbig 1960), using infrared spectroscopy. We restrict our study to a sub-group of mostly late B and A-F type stars (hereafter HAe stars). These stars show little or no optical extinction and low mass accretion rates, as derived from radio analysis

Send offprint requests to: R. van Boekel (vboekel@science.uva.nl)

* Based on observations obtained at the European Southern Observatory (ESO), La Silla, observing programmes 68.C-0536 and 70.C-0533, and on observations with ISO, an ESA project with instruments funded by ESA Member States (especially the PI countries: France, Germany, the Netherlands and the United Kingdom) and with the participation of ISAS and NASA.

(Skinner et al. 1993), and the lack of significant veiling in optical spectra. For these lower mass members of the Herbig class, evidence for the disk hypothesis is compelling (e.g. Mannings & Sargent 1997; Grady et al. 2001; Augereau et al. 2001; Eisner et al. 2003).

The observed SEDs of these HAe stars can very well be explained with models for gas-rich, passively heated disks in hydrostatic equilibrium and a puffed-up inner rim (Dullemond et al. 2001). These models indicate that the emission observed at near-IR wavelengths is dominated by the inner rim, while the mid-IR spectrum has a large contribution from the dust grains in the warm surface layers of the disk, typically located between a few to several tens of Astronomical Units (AU) from the star. Therefore, mid-IR spectroscopy predominantly relates to the composition of the dust in this surface layer. Van Boekel et al. (2003) argue that due to the turbulent nature of the disks, the small grains observed at the disk surface are well coupled to those in the disk mid-plane, and so the observations of the surface layers likely bear relevance for the overall small grain population.

Observations of the dust composition in HAe disks have revealed a very rich mineralogy, and strong source to source variations of the dust composition (e.g. Bouwman et al. 2001). Some stars show strong 9.7 and 18 μm amorphous silicate emission, with a band shape and strength very similar to that seen in the interstellar medium. Other objects have only weak silicate emission, with sub-structure at 9.2, 10.6 and 11.3 μm due to crystalline silicates. At longer wavelengths, high-quality observations only exist for a small number of stars, so far all obtained with the Infrared Space Observatory (ISO). This situation is rapidly improving due to ongoing observations with the Infrared Spectrograph on board of the Spitzer Space Telescope. The ISO spectra reveal a mineralogy dominated by the crystalline silicates forsterite and enstatite, i.e. Mg-rich, Fe-poor materials (e.g. Malfait et al. 1998b; Bouwman et al. 2001; Meeus et al. 2001, hereafter ME01). A small group of stars lacks silicate emission, but shows prominent emission from Polycyclic Aromatic Hydrocarbons (PAHs) at 3.3, 6.2, 7.7-7.9, 8.6 and 11.3 μm . Many stars show a combination of silicates and PAHs.

In recent years, several investigators have attempted to find correlations between the properties of the dust in the disk of Herbig stars on the one hand, and global properties of the disk (e.g. disk geometry) and/or the star (e.g. mass, luminosity, age, binarity) on the other hand (ME01; Bouwman et al. 2001; Acke & van den Ancker 2004). Perhaps the most promising results so far are relations between the dust properties and the shape of the SEDs of the disk; for instance, the PAH bands are on average stronger in sources with SEDs that rise at far-IR wavelengths (ME01). This has been interpreted in terms of the disk geometry in the following way. Relatively red SEDs correspond to flaring disks, that have a large surface which is directly irradiated by the star. If PAHs are present in this flaring disk surface layer, they will contribute to the emission in the familiar PAH bands. Van Boekel et al. (2004b) studied the spatial distribution of the PAH emission in

HD 97048, which was found to be extended on a scale of 1-2 arcsec (~ 250 AU) but clearly associated with the disk. It is likely that also in the other stars of our sample, the PAH emission originates from the outer disk region. Disks that lack a flaring outer region will have much less prominent PAH emission. Acke & van den Ancker (2004) confirm this relation between PAH band strength and SED shape using a sample of about 50 Herbig Ae/Be stars. Acke et al. (2004) note that stars with flat far-IR SEDs on average have flat millimeter spectral slopes, suggesting that the cold mid-plane grains in these sources have grown to larger size than the corresponding grains of stars with rising far-IR SEDs.

Despite considerable efforts, it has proven difficult so far to determine relations between stellar and dust parameters. This has prompted us to carry out a comprehensive spectral survey at $10\ \mu\text{m}$ of isolated HAe stars. Our goal is to establish relations between star and dust properties that are of relevance for our understanding of the evolution of dusty disks around young stars, by increasing the number of stars for which mid-IR spectra are available. We have used the *Thermal Infrared Multi Mode Instrument 2* (TIMMI2, Reimann et al. 1998), attached to the 3.6 m telescope of the European Southern Observatory for our spectral survey. All known optically bright HAe stars accessible from the La Silla observatory were included in our initial list of targets. In practice, high quality data could be obtained for stars with $10\ \mu\text{m}$ fluxes of about 3 Jy or more.

Here we present the results of our spectroscopic survey at $10\ \mu\text{m}$. In total, we obtained high quality spectra of a sample of 24 HAe stars, introduced in section 2. We report on the observations and data reduction in section 3. An overview of the spectra is given in section 4. In section 5 we present compositional fits to the silicate feature observed in most of the sources, using the optical properties of minerals commonly found in circumstellar disks. In section 6 we discuss the implications of our results for our understanding of dust processing in HAe disks.

2. The sample stars

Our sample of stars was selected from a larger list of (candidate) Herbig Ae/Be stars studied by Malfait et al. (1998a). This list was constructed by comparing the positions of stars in the Smithsonian Astrophysical Observatory Star Catalog with positions in the Infrared Astronomical Satellite (IRAS) point source catalogue, and subsequent follow-up studies to find the Herbig star candidates. Clearly, such a way to select stars may introduce biases. Our sample does not contain stars that are heavily obscured due to e.g. on-going accretion or an edge-on dusty disk. Instead, our sample is dominated by stars with a relatively “clean” environment, low optical extinction, and disk orientations that are not close to edge-on. An overview of the stars in the sample and their basic parameters is given in Table 1.

In order to select “genuine” HAe stars, we applied the following selection criteria:

Table 1. Basic parameters of the sample stars. In columns 1 and 2 we give the index number by which a star can be identified in tables and figures throughout this work, and the name of the star, respectively. The classification of the sources according to ME01 is listed in the third column. In column 5 the distances, derived from direct (Hipparcos) parallax measurements or by association to a star forming region (SFR, column 4), are given. For the stars where the distance is determined by association with a SFR we assume an error of 30 % in the distance. The spectral type according to the MK classification, the effective temperature and the stellar luminosity are given in columns 6, 7 and 8, respectively. Mass and age estimates for most stars, as derived by comparing their positions in the HR diagram to theoretical pre-main-sequence tracks, are given in columns 9 and 10. For HD 101412 we have no reliable distance estimate, and can therefore not determine its luminosity, mass and age.

(1)	(2)	(3)	(4)	(5)	(6)	(7)	(8)	(9)	(10)
#	star	group	SFR	d [pc]	Sp.Type	log T _{eff} [K]	log L [L _⊙]	Mass [M _⊙]	log(Age) [yr]
1	AB Aur	Ia	L519	144 ⁺²² ₋₁₇	A0Ve+sh	3.979	1.67	2.4±0.2	6.3±0.2
2	UX Ori	IIa	Orion OB1a	340 ± 102	A4IVe	3.925	1.68	2.5±0.3	6.3±0.4
3	HD 36112	Ia		204 ⁺⁶³ ₋₃₉	A5IVe	3.911	1.35	2.0±0.3	6.5±0.3
4	HK ORI	IIa	Orion OB1a	340 ± 102	A4pevar	3.927	0.87	1.7±0.3	>6.8
5	HD 245185	Ia	Orion OB1a	340 ± 102	A0Ve	3.979	1.26	2.2±0.3	>6.8
6	V380 Ori	IIa	Orion OB1c	510 ± 153	A1:e	3.965	1.88	2.8±0.5	6.2±0.4
7	HD 37357	IIa		240 ± 72 ¹	A2Ve	4.021	1.47	2.4±0.4	>7.0
8	HD 37806	IIa	Orion OB1b	470 ± 141	A2Vpe	3.953	2.13	3.6±0.8	5.9±0.4
9	HD 95881	IIa	Sco OB2-4?	118 ± 35	A2III/IVe	3.954	0.88	1.7±0.2	>6.5
10	HD 97048	Ib	Ced 111	175 ⁺²⁶ ₋₂₀	B9.5Ve+sh	4.000	1.64	2.5±0.2	>6.3
11	HD 100453	Ib		111 ⁺¹⁰ ₋₈	A9Ve	3.869	0.90	1.7±0.2	7.0±0.1
12	HD 100546	Ia	Sco OB2-4?	103 ⁺⁶ ₋₆	B9Vne	4.021	1.51	2.4±0.1	>7.0
13	HD 101412	IIa			B9.5V				
14	HD 104237	IIa	Cha III	116 ⁺⁷ ₋₆	A4IVe+sh	3.925	1.54	2.3±0.1	6.3±0.1
15	HD 135344	Ib	Sco OB2-3	140 ± 42	F4Ve	3.819	0.91	1.6±0.2	6.9±0.3
16	HD 139614	Ia	Sco OB2-3	140 ± 42	A7Ve	3.895	0.91	1.7±0.3	>7.0
17	HD 142666	IIa	Sco OB2-2	145 ± 43	A8Ve	3.880	1.13	1.8±0.3	6.8±0.4
18	HD 142527	Ia		198 ⁺⁶⁰ ₋₃₇	F7IIIe	3.796	1.46	2.5±0.3	6.0±0.4
19	HD 144432	IIa	Sco OB2-2	145 ± 43	A9IVev	3.866	1.01	1.8±0.2	7.0±0.3
20	HD 144668	IIa	Lupus 3	207 ⁺⁴⁵ ₋₃₁	A5-7III/IVe	3.899	1.94	3.2±0.5	5.7±0.3
21	HD 150193	IIa	Sco OB2-2	150 ⁺⁵⁰ ₋₃₀	A2IVe	3.953	1.38	2.3±0.2	>6.3
22	HD 163296	IIa		122 ⁺¹⁶ ₋₁₃	A3Ve	3.941	1.38	2.0±0.2	6.7±0.4
23	HD 169142	Ib	Sco OB2-1	145 ± 43	A5Ve	3.914	1.16	2.0±0.3	6.9±0.3
24	HD 179218	Ia	(L693)	243 ⁺⁶⁸ ₋₄₃	B9e	4.021	2.00	2.9±0.5	6.1±0.4

¹ We adopted a distance of 240 pc so that the luminosity of this star matches its spectral type.

1. The position in the HR diagram should be in agreement with that of a pre-main-sequence (PMS) star with a mass between 1.5 and 3.5 M_⊙ (see Fig. 1).
2. The color criterion J-H>0.25 mag, assuring that the onset of the near-infrared (NIR) excess is well defined, in agreement with the inner boundary of the gas rich disk being

Table 2. Literature infrared photometry used in this work. Columns 3-7 list the magnitudes in the J ($1.25\mu\text{m}$), H ($1.65\mu\text{m}$), K ($2.2\mu\text{m}$), L ($3.6\mu\text{m}$), and M ($4.8\mu\text{m}$) photometric bands, with references in column 8. The listed reference codes are: BO: Bouchet et al. 1991; CA: Carter 1990; CO: Cohen 1973; CU: Cutri et al. 2003; DW: de Winter et al. 2001; DW2: de Winter et al. 1996; EI: Eiroa et al. 2001; FO: Fouque et al. 1992; GL: Glass & Penston 1974; HI: Hillenbrand et al. 1992; LA: Lawrence et al. 1990; MA: Malfait et al. 1998a; ME: Mendoza 1967; ST: Strom et al. 1990; SY: Sylverster et al. 1996; VR: Vrba et al. 1976; WA: Waters et al. 1988. Columns 9-12 contain the infrared fluxes in Jy from the IRAS Point Source Catalogue (Joint IRAS Science Working Group 1988).

(1)	(2)	(3)	(4)	(5)	(6)	(7)	(8)	(9)	(10)	(11)	(12)
#	star	J	H	K	L	M	references	$12\mu\text{m}$	$25\mu\text{m}$	$60\mu\text{m}$	$100\mu\text{m}$
1	AB Aur	6.10	5.10	4.40	3.30	2.90	HI	27.16	48.10	105.60	114.10
2	UX Ori	8.03	7.43	6.71	5.61	5.32	DW,26.2.1986	2.68	3.69	2.85	~ 3.76
3	HD 36112	7.44	6.70	5.90	4.75	4.47	MA	5.59	12.59	27.98	18.95
4	HK Ori	9.52	8.38	7.29	5.87	5.10	HI	3.80	4.08	<1.64	<70.37
5	HD 245185	9.34	8.87	8.26	7.46	6.23	HI	4.00	5.96	4.97	3.61
6	V380 Ori	8.25	7.10	6.03	4.44	3.61	J-L ST; M ME	8.61	8.85	<75.90	<38.59
7	HD 37357	8.31	7.88	7.24	6.33		MA	2.01	2.79	~ 2.90	~ 20.29
8	HD 37806	7.38	6.68	5.77	4.23	3.79	MA	11.02	9.40	<5.18	<33.98
9	HD 95881	7.50	6.79	5.87	4.28	3.71	MA	9.14	6.87	1.45	<1.09
10	HD 97048	7.30	6.75	6.04	4.61	4.56	HI	14.49	40.34	69.91	<250.10
11	HD 100453	6.97	6.32	5.52	4.20	3.79	MA	7.23	33.59	39.36	23.86
12	HD 100546	6.43	5.88	5.20	4.15	3.80	MA	65.78	242.60	165.20	98.56
13	HD 101412	8.70	8.24	7.25	5.81	5.08	DW	3.22	3.09	~ 1.69	~ 10.52
14	HD 104237	5.75	5.14	4.42	3.05	2.58	MA	23.65	23.05	14.72	9.58
15	HD 135344	7.44	6.72	5.96	4.76	4.69	MA	1.59	6.71	25.61	25.69
16	HD 139614	7.75	7.34	6.76	5.68	5.49	MA	4.11	18.14	19.30	13.94
17	HD 142666	7.34	6.72	6.04	4.97	4.69	MA	8.57	11.21	7.23	5.46
18	HD 142527	6.65	5.94	5.20	3.89	3.50	MA	10.38	21.23	105.10	84.70
19	HD 144432	7.21	6.69	6.14	5.14	4.90	MA	7.53	9.36	5.76	3.29
20	HD 144668	5.83	5.18	4.38	3.08	2.54	HI	18.05	14.51	~ 14.36	<63.25
21	HD 150193	7.05	6.37	5.64	4.37	3.93	MA	17.61	18.10	8.13	<16.25
22	HD 163296	6.24	5.52	4.70	3.52	3.14	MA	18.20	20.99	28.24	<40.62
23	HD 169142	7.43	7.01	6.53	5.64	5.57	MA	2.95	18.43	29.57	23.42
24	HD 179218	6.99	6.64	5.91	4.68	4.18	J,H EI; K-M LA	23.44	43.63	29.92	17.35

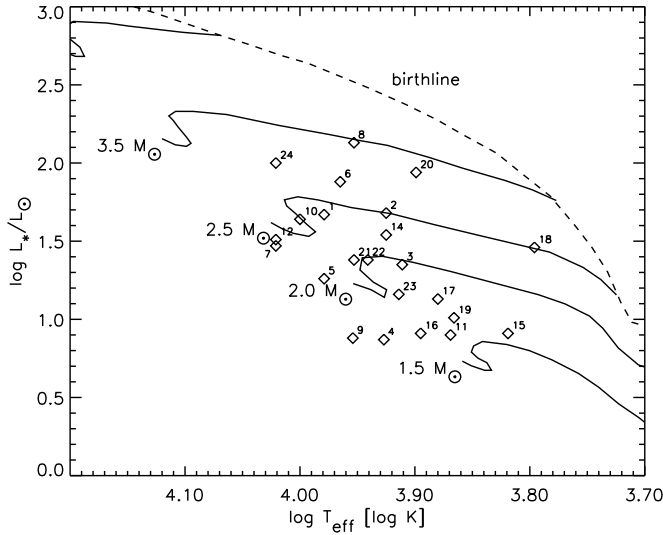


Fig. 1. The positions of our stars in the HR diagram. The solid curves indicate the pre-main sequence evolutionary tracks of stars of different masses; the dashed curve represents the birthline for an accretion rate of $10^{-5} M_{\odot} \text{yr}^{-1}$ (both are taken from Palla & Stahler 1993).

set by the silicate evaporation temperature of $\sim 1500 \text{ K}$ (see Table 2 for an overview of the photometric data used).

2.1. Selection effects

In order to identify if other selection effects may have entered our sample, we determined the mass and age (calculated from the birthline, for an accretion rate of $10^{-5} M_{\odot} \text{yr}^{-1}$) of the stars by placing them in the HR diagram (Fig. 1) and comparing their positions to PMS evolutionary tracks published by Palla & Stahler (1993). Throughout this work “(PMS) age” τ is defined as the time that past since the star was on the birthline, which is when the star becomes optically visible for the first time. The luminosity is calculated from the observed photometry and the measured distance to each star. The uncertainties in the derived stellar masses and ages listed in Table 1 and shown in Fig. 2 mainly reflect the uncertainty in the distances (see also van den Ancker et al. 1998). A comparison of the stellar parameters derived using the Palla & Stahler (1993) evolutionary tracks to those obtained using more recent calculations (Palla & Stahler 1999; Siess et al. 2000), shows that the particular choice of PMS tracks introduces an additional uncertainty in the stellar ages that is of the same order as those implied by observational uncertainties in the position of the star in the HR diagram. This additional uncertainty is not taken into account. In Fig. 2 we show the derived stellar masses versus the PMS ages of the stars. It is evident from this figure that our sample lacks “old” ($\tau \gtrsim 10^{6.3} \text{ yr}$) disks around $3\text{-}4 M_{\odot}$ stars, and “young” ($\tau \lesssim 10^6 \text{ yr}$) disks around stars less massive than about $2.5 M_{\odot}$. The

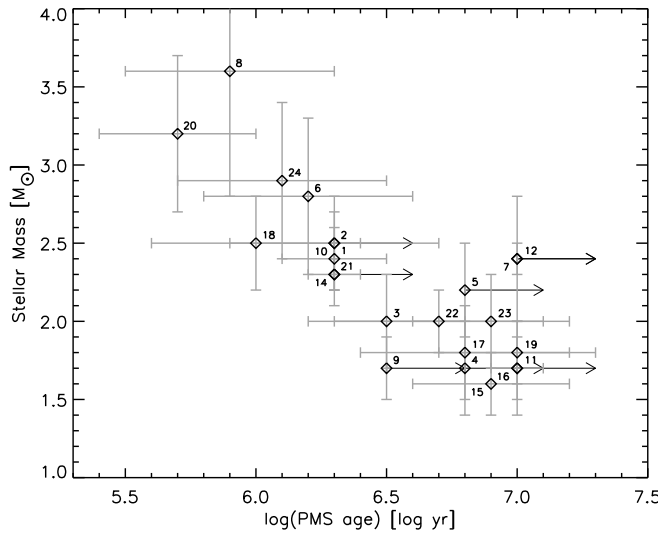


Fig. 2. The derived stellar mass estimates vs. the pre-main-sequence age estimates derived from a comparison of their position in the HR diagram to PMS evolutionary tracks of Palla & Stahler (1993). Our sample shows a clear lack of disks around relatively old stars of $3-4 M_{\odot}$, and of disks around relatively young stars less massive than about $2.5 M_{\odot}$.

lack of “old” disks around $3-4 M_{\odot}$ stars is likely caused by the shorter timescale on which the disks around more massive stars are dispersed. It is therefore not a selection effect. The lack of “young” disks around the lower mass stars is most likely caused by the fact that these stars do not clear their environment as rapidly as the more massive (more luminous) stars, and consequently become optically bright later in their evolution. Also, at a given age, lower mass PMS stars are less luminous than more massive ones, and so more easily escape optical detection. This selection effect must be taken into account in any discussion about the evolution of the dust in proto-planetary disks based on optically selected samples.

2.2. Classification of the sources

ME01 empirically decomposed the infrared spectra of Herbig Ae/Be stars into three components: a power law component, a cold black-body component, and solid state emission bands (mainly at 10 and $20 \mu\text{m}$). They found that some sources exhibit both the power law and cold black-body component, and classified these sources as “group I”. Sources that lack the cold black-body component were classified as “group II”. A further division into subgroups “a” and “b” serves to indicate the presence or absence, respectively, of silicate emission bands at 10 and $20 \mu\text{m}$. It was proposed by ME01 that group I sources have a large (several hundred AU) flared outer disk, whereas the group II sources have a smaller, non-flaring outer disk.

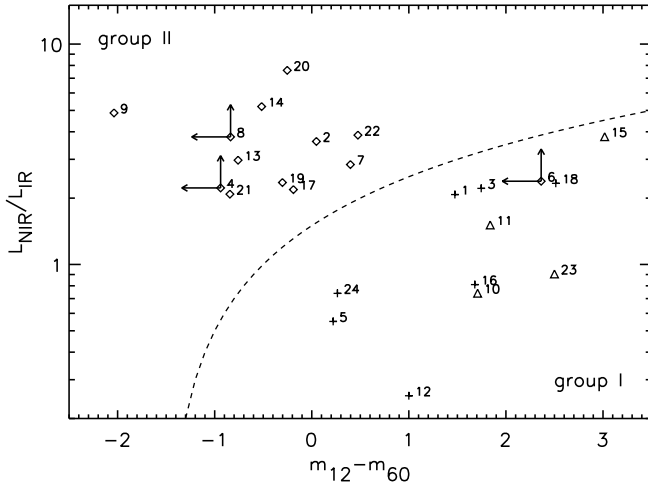


Fig. 3. Classification of the sources based on global SED properties. We plot the ratio of the near-infrared and infrared luminosity (see section 2.2) vs. the IRAS $m_{12}-m_{60}$ color (defined as $m_{12}-m_{60} = -2.5 \log \mathcal{F}_{12}/\mathcal{F}_{60}$, where \mathcal{F}_{12} and \mathcal{F}_{60} are the fluxes at 12 and 60 μm as listed in the IRAS point source catalogue). Sources classified as group I according to ME01 are in the lower right part of the diagram, group II sources are in the upper left part. Group Ia sources are indicated with crosses, group Ib sources by triangles, and group II sources with diamonds. The dashed curve indicates our division line between the two groups (section 2.2).

We classify the sources for which we have newly measured N-band (8-13.5 μm) spectra following ME01. Whereas ME01 had ISO spectra of their sources at their disposal, our classification is based solely on broad-band photometry. We find that the group I and group II sources are well separated in an IRAS $m_{12}-m_{60}$ color versus $L_{\text{NIR}}/L_{\text{IR}}$ diagram (Fig. 3), where L_{NIR} is the integrated luminosity as derived from the J,H,K,L and M band photometry, and L_{IR} is the corresponding quantity derived from the IRAS 12, 25 and 60 μm points. For group I sources, $L_{\text{NIR}}/L_{\text{IR}} \leq (m_{12}-m_{60})+1.5$, group II sources have $L_{\text{NIR}}/L_{\text{IR}} > (m_{12}-m_{60})+1.5$. The dashed line in Fig. 3 indicates the boundary between the two groups. To avoid any pre-assumptions concerning the spectral shapes of our targets, we did not apply color correction to the IRAS data for the classification of the sources.

By use of the $L_{\text{NIR}}/L_{\text{IR}}$ ratio (van Boekel et al. 2003) we compare the near-IR SED to the mid-IR SED. The near-IR SED is found to be similar for all HAe stars (Natta et al. 2001), while the major differences occur in the mid-IR SED. The $L_{\text{NIR}}/L_{\text{IR}}$ ratio is smaller for group I than for group II sources. The mid-IR SED of group I sources is “double-peaked” compared to the SED of a group II source. Group I sources are redder than their group II counterparts. The IRAS $m_{12}-m_{60}$ color index quantifies this difference in SED shape.

Table 3. Log of the TIMMI2 observations. We list the observing date (defined as the day on which each observing night began), time (U.T.), airmass of the observation, and integration time in seconds (columns 3-6). The calibrators used for the atmospheric correction are also given, with the time and airmass of the measurements (columns 7-12).

(1)	(2)	(3)	(4)	(5)	(6)	(7)	(8)	(9)	(10)	(11)	(12)
#	star	date	time	m_A	T_{int}	calibrator 1	time	$m_{A,1}$	calibrator 2	time	$m_{A,2}$
2	UX Ori	27-12-2001	01:09	1.31	1380	HD 32887	01:59	1.06	HD 32887	00:39	1.25
3	HD 36112	18-03-2003	23:19	1.83	960	HD 48915	00:27	1.04	HD 29139	23:58	1.88
4	HK Ori	19-03-2003	23:21	1.39	960	HD 48915	00:56	1.08	HD 23249	00:04	1.68
5	HD 245185	19-03-2003	00:27	1.56	720	HD 48915	00:56	1.08	HD 23249	00:04	1.68
6	V380 Ori	17-03-2003	00:59	1.37	960	HD 48915	00:21	1.04	HD 58972	01:36	1.34
7	HD 37357	19-03-2003	01:08	1.43	720	HD 48915	00:56	1.08	HD 55865	02:33	1.46
8	HD 37806	27-12-2001	04:04	1.12	690	HD 32887	01:59	1.06	HD 32887	00:39	1.25
9	HD 95881	17-03-2003	02:55	1.37	720	HD 48915	00:21	1.04	HD 107446	02:41	1.32
10	HD 97048	19-03-2003	03:02	1.52	720	HD 98292	04:02	1.28	HD 55865	02:33	1.46
11	HD 100453	18-03-2003	05:24	1.13	960	HD 93813	05:00	1.08	HD 146003	06:38	1.25
12	HD 100546	19-03-2003	05:09	1.34	960	HD 109379	05:36	1.01	HD 98292	06:18	1.37
13	HD 101412	17-03-2003	03:25	1.19	960	HD 48915	00:21	1.04	HD 89388	04:04	1.19
14	HD 104237	17-03-2003	04:57	1.52	480	HD 123139	08:04	1.03	HD 89484	04:37	1.65
15	HD 135344	17-03-2003	05:56	1.13	960	HD 123139	08:04	1.03	HD 107446	06:35	1.20
16	HD 139614	17-03-2003	07:25	1.05	960	HD 123139	08:04	1.03	HD 107446	06:35	1.20
17	HD 142666	18-03-2003	06:07	1.23	720	HD 93813	05:00	1.08	HD 146003	06:38	1.25
18	HD 142527	18-03-2003	06:56	1.11	720	HD 123139	08:07	1.04	HD 146003	06:38	1.25
19	HD 144432	18-03-2003	07:25	1.06	960	HD 123139	08:07	1.04	HD 146003	06:38	1.25
20	HD 144668	17-03-2003	09:15	1.02	720	HD 152334	09:45	1.03	HD 152786	09:01	1.14
21	HD 150193	18-03-2003	08:23	1.04	720	HD 123139	08:07	1.04	HD 146003	06:38	1.25
22	HD 163296	18-03-2003	09:40	1.04	480	HD 123139	08:07	1.04	HD 152786	09:22	1.12
23	HD 169142	17-03-2003	10:07	1.03	960	HD 152334	09:45	1.03	HD 152786	09:01	1.14
24	HD 179218	19-03-2003	09:39	1.78	480	HD 152334	07:59	1.10	HD 187642	10:00	1.68

3. Observations and data reduction

Infrared spectra in the $10\mu\text{m}$ atmospheric window were taken in December 2001 and March 2003 with the TIMMI2 instrument mounted at the 3.60 m telescope at ESO La Silla observatory. Conditions were clear during all nights. The low resolution ($R \approx 160$) N band grism was used in combination with a 1.2 arcsecond slit. The pixel scale in the spectroscopic mode of TIMMI2 is 0.45 arcseconds. A log of our observations is given in Table 3.

3.1. Atmospheric correction

Ground-based observations at $10\mu\text{m}$ are particularly challenging because of the high atmospheric and instrumental background, and the varying transmission of the earth atmosphere. As proper spectral calibration is essential for the compositional analysis presented in section 5.1, we report here in some detail on our data reduction method.

To deal with the high background signal, we employed standard chopping and nodding, using a $+10$ arcsecond chop throw North-South, and a -10 arcsecond nod throw North-South. For the spectral calibration of our measurements we regularly observed standard stars. These observations are used to determine both the atmospheric extinction per unit airmass (A_ν) and the instrumental response (R_ν) at all wavelengths. For each science observation, we determine A_ν and R_ν from two calibration measurements:

$$\begin{aligned} s_{\nu,1} &= I_{\nu,1} e^{-\tau_{\nu,1}} R_\nu; & \tau_{\nu,1} &= A_\nu m_{A,1} \\ s_{\nu,2} &= I_{\nu,2} e^{-\tau_{\nu,2}} R_\nu; & \tau_{\nu,2} &= A_\nu m_{A,2}, \end{aligned} \quad (1)$$

where $s_{\nu,i}$ are the measured calibrator spectra, $I_{\nu,i}$ are the intrinsic (model) calibrator spectra, $\tau_{\nu,i}$ are the optical depths of the earth atmosphere during the calibration measurements, and $m_{A,i}$ denote the airmass at which the calibrators were observed. Whenever possible, we chose $m_{A,1}$ or $m_{A,2}$ to be very close to the airmass of the science observation. Both calibrator measurements are chosen as close in time as possible to the science observation. For the intrinsic calibrator spectra we use “spectral templates” by Cohen et al. (1999)¹. Table 4 lists the observed calibrators and the applied templates, which are chosen to match the calibrator spectral type as closely as possible. Solving Eq. 1 for A_ν and R_ν , we find:

$$A_\nu = \frac{\ln(I_{\nu,2}/I_{\nu,1}) + \ln(s_{\nu,1}/s_{\nu,2})}{m_{A,2} - m_{A,1}} \quad (2)$$

$$R_\nu = \frac{s_{\nu,1}}{I_{\nu,1} e^{-A_\nu m_{A,1}}} \quad (3)$$

The intrinsic spectrum of a science target observed at airmass m_A is then calculated from its measured spectrum s_ν as:

$$I_\nu = \frac{s_\nu}{R_\nu} e^{A_\nu m_{rmA}} \quad (4)$$

For a number of sources we have ISO spectra available. We generally find very good agreement in spectral shape between the ISO data and our new ground based spectra. A comparison with the ISO spectra of the brighter stars (HD 100546, HD 163296, HD 150193) shows differences at the level of at most a few percent in the shape of the

¹ available for download at the TIMMI2 website (<http://www.ls.eso.org/lasilla/sciops/timmi/docs/tables/>)

spectra, when the TIMMI2 spectra are scaled such as to most closely match the flux levels in the ISO spectra. For each HAe star spectrum, the time and airmass of observation, as well as the time and airmass of the two calibration observations are given in Table 3.

3.2. Flux calibration

Our stars have been selected to be *isolated* Herbig stars. Therefore, the IRAS photometry will in most cases not be contaminated by emission from nearby sources or a surrounding remnant cloud. All emission seen in the IRAS data is expected to originate in the disk. We flux-calibrated the spectra using the IRAS 12 μm data, by applying a scaling factor q such that

$$q \int_{\nu=0}^{\infty} I_{\nu} T_{\nu} d\nu = \mathcal{F}_{12} \times 1.35 \times 10^{-10} \quad [\text{erg s}^{-1}\text{cm}^{-2}], \quad (5)$$

where T_{ν} is the normalized instrumental response function of the IRAS 12 micron band, and \mathcal{F}_{12} is the 12 micron flux as listed in the IRAS point source catalogue (a source that has a 12 μm flux of $\mathcal{F}_{12}=1$ Jy in the IRAS point source catalogue, yields an inband flux of 1.35×10^{-10} erg $\text{s}^{-1}\text{cm}^{-2}$). The IRAS 12 micron band runs from 8 to 15 μm and is therefore somewhat broader than our spectral coverage. To allow for the calibration we estimate the spectrum between 13.5 and 15 μm , by linearly extrapolating I_{ν} between the continuum points measured at 8 and 13 μm . Our final calibrated spectrum is then $F_{\nu} = qI_{\nu}$. We estimate the absolute photometric accuracy to be 15%.

4. Description of the observations

4.1. Description of the spectra

The spectra of our sample of HAe stars are shown in Fig. 4. All stars show spectral structure on top of a continuum whose slope varies strongly from star to star. The spectral features are due to various kinds of silicates (see section 5.1 below). Also, emission from Polycyclic Aromatic Hydrocarbons (PAHs) can be seen, at 7.9, 8.6, 11.3 and 12.7 μm . The relative importance of the silicate and PAH contributions varies strongly. There are sources that show both silicate and PAH emission (e.g. HD 100546, HD 179218), sources that show only silicate emission (e.g. HD 144432), and sources that display only PAH emission (these are the group Ib sources HD 97048, HD 100453, HD 135344, and HD 169142). There are no sources in our sample that have a completely featureless 10 micron spectrum.

ME01 and Acke & van den Ancker (2004) found that the SED correlates with the presence and/or strength of the PAH bands: group I sources tend to show (prominent) PAH emission, while group II sources do not. This trend is confirmed in our sample, but we note that there is considerable scatter. For instance, HD 95881 has little far-IR excess and is thus classified as group II, but, nonetheless, shows clear PAH emission bands.

Table 4. Spectral templates used for the calibrators (see section 3.1).

calibrator	spectral type	template file	template sp. type
HD 23249	K0IV	hd123139.tem	K0IIIb
HD 29139	K5III	alp_Tau.dat	K5III
HD 48915	A1V	ν^2 law	ν^2 law
HD 55865	K0III	hd123139.tem	K0IIIb
HD 58972	K3III	hd6805.tem	K2III
HD 89388	K3IIa	hd6805.tem	K2III
HD 89484	K1IIIb	hd169916.tem	K1IIIb
HD 92397	K4.5III	hd32887.tem	K4III
HD 93813	K0/K1III	hd123139.tem	K0IIIb
HD 98292	M2III	alp_Tau.dat	K5III
HD 107446	K3.5III	hd32887.tem	K4III
HD 109379	G5II	hd37160.tem	G8III-IV
HD 123139	K0IIIb	hd123139.tem	K0IIIb
HD 146003	M2III	alp_Tau.dat	K5III
HD 152334	K4III	hd32887.tem	K4III
HD 152786	K3III2	hd6805.tem	K2III
HD 177716	K1IIIb	hd169916.tem	K1IIIb
HD 187642	A7V	HD187642_spec.dat	A7IV-V

The silicate band shows very large variations in shape and strength. The bulk of the emission is in most cases due to amorphous silicates, but almost all stars show some spectral structure near $11.3\mu\text{m}$, which can be attributed to forsterite. Note, however, that this feature blends with the $11.3\mu\text{m}$ PAH band. There are also prominent narrow emission bands near 9.2 and $10.6\mu\text{m}$. These are due to crystalline enstatite. The spectrum of HD 100546 is dominated by crystalline forsterite, while that of HD 179218 is dominated by crystalline enstatite. This latter star shows one of the richest $10\mu\text{m}$ spectra observed to date (see Fig.5). The resonances of crystalline enstatite are clearly visible in the spectrum of this source. The ISO spectrum of HD 179218 at longer wavelengths also points to a relatively high abundance of crystalline enstatite (Bouwman et al. 2001). It is obvious that the nature of the crystalline dust in our sample shows very large variations, both in terms of the fraction of the dust that is crystalline, and in composition.

There are four stars (HD 97048, HD 100453, HD 135344 and HD 169142), all classified as group I, that show no detectable silicate emission. Instead, their $10\mu\text{m}$ spectra are dominated by PAH emission. The lack of silicate emission is most simply explained by assuming that there are no small ($< 3\text{-}5\mu\text{m}$) silicate grains in the inner 10-20 AU of the disk. Meeus et al. (2002) derive limits on the presence of small silicate grains in

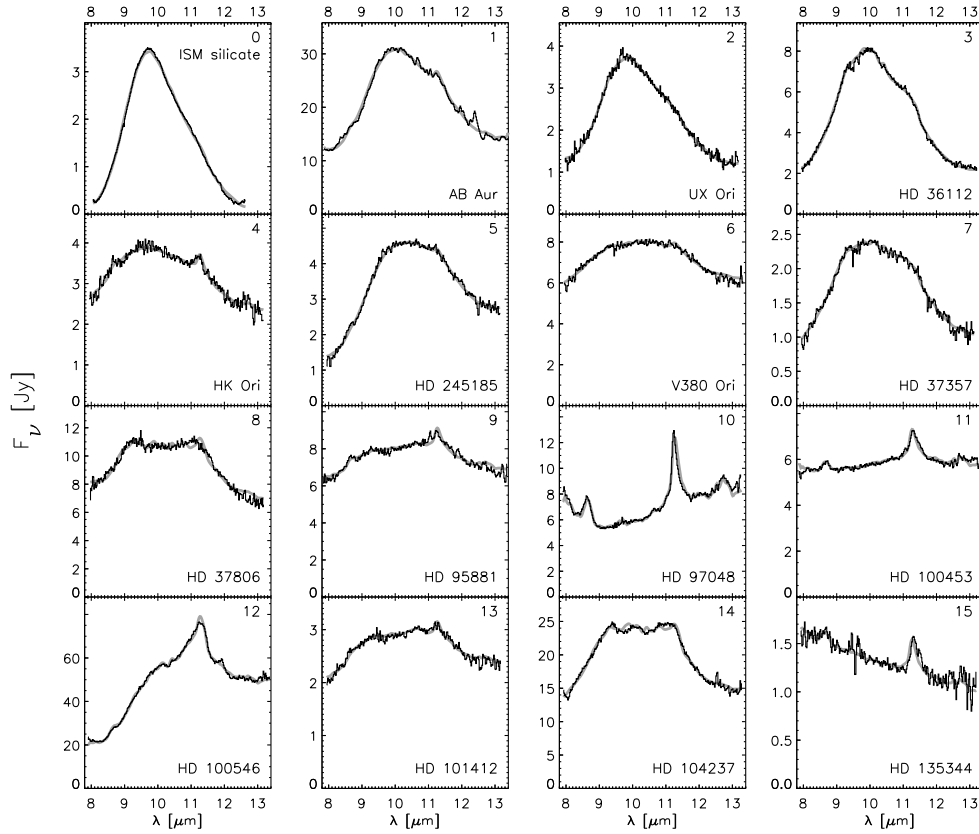


Fig. 4. N-band spectra of the sources in our sample. The ISM silicate extinction efficiency, plotted in the upper left panel, was taken from Kemper et al. (2004). The AB Aur spectrum was taken by ISO (van den Ancker et al. 2000). Also plotted are the best fits to the spectra (grey curves, see section 5.2).

HD 100453, and argue that all grains smaller than $4\mu\text{m}$ must have been removed. The most likely cause for the removal of small silicate grains is grain growth, but apparently this has not affected the population of small carbonaceous grains to the same extent (van Boekel et al. 2004b). Possibly, small grains survive in the outer disk regions. At large distance from the star, the silicate grains may be too cold to contribute to the $10\mu\text{m}$ spectrum, while the PAHs can still produce significant emission. This can only occur if the PAHs have not been incorporated into larger grains. Indeed, van Boekel et al. (2004a) find evidence for a distance dependence of the typical silicate grain size in the surface layers of HAe star disks: in the innermost regions growth has proceeded further than in the outer disk regions.

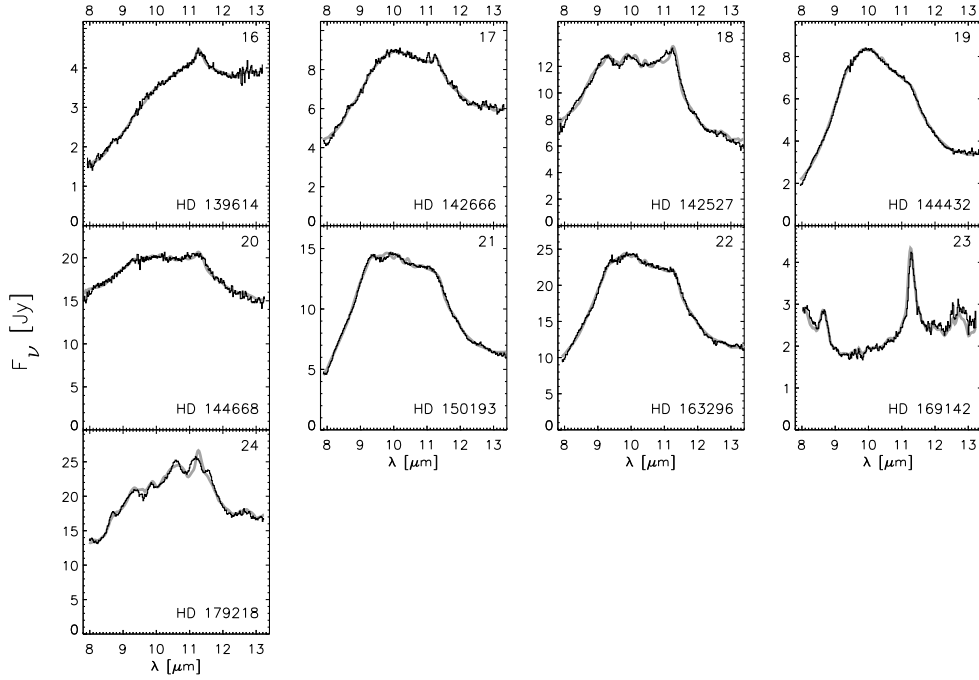


Fig. 4. (Continued)

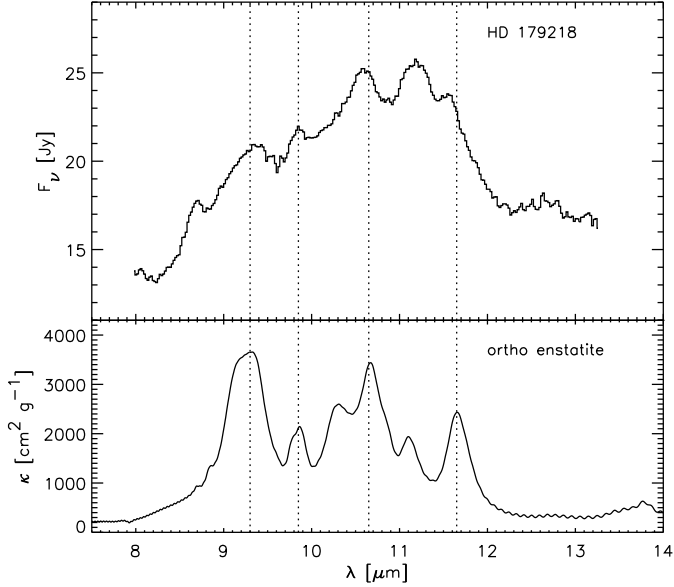


Fig. 5. The N-band spectrum of HD 179218 (upper panel), and the measured mass absorption coefficients of ortho enstatite taken from Chihara et al. (2002) (lower panel). The wavelengths of the most prominent emission bands are indicated by the dotted lines. In this object, enstatite grains are an important constituent of the grain population that causes the $10\mu\text{m}$ feature.

4.2. The shape and strength of the silicate feature

In Fig. 6 we show the ratio of the continuum subtracted flux at 11.3 and $9.8\mu\text{m}$, against the silicate peak to continuum ratio (“feature strength”)². Group I sources are indicated

² To estimate the continuum we simply interpolate linearly between 8 and 13 micron. The peak/continuum ratio is the maximum value of the normalized spectrum $F_{norm} = 1 + F_{\nu,cs} / <$

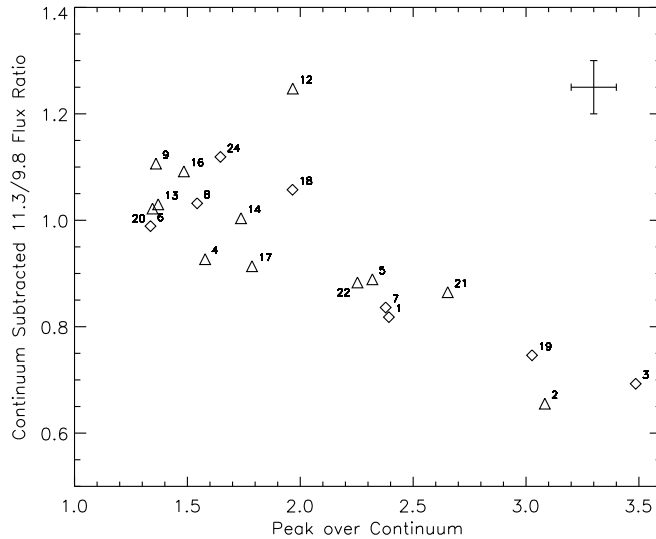


Fig. 6. The flux ratio of the continuum subtracted spectra at 11.3 and 9.8 micron (a measure for the amount of processing that the material has undergone) versus the peak/continuum ratio of the silicate feature (a measure for the typical grain size). Group I sources are represented by triangles, group II sources by diamonds. In the upper right corner of the figure we have indicated the typical uncertainties in the displayed quantities.

with triangles, group II sources with diamonds (the “outlier” # 12 is HD 100546). Sources with a low 11.3/9.8 ratio have a triangular shaped emission feature, clearly peaked just shortward of 10 μm (e.g. UX Ori, in Fig. 4). Sources with a high 11.3/9.8 generally have a broad, flat-topped emission band, often showing substructure (e.g. HD 37806, HD 142527). There is a clear correlation between the shape and strength of the silicate feature; stars with a strong feature (i.e. a high peak/continuum ratio) have a low 11.3/9.8 ratio, whereas stars with weaker silicate features have higher 11.3/9.8 ratios. This correlation was first demonstrated in Herbig Ae stars by van Boekel et al. (2003). Meeus et al. (2003) and Przygoda et al. (2003) have subsequently shown that the same trend is observed in the silicate feature of T-Tauri stars.

The shape of the emission bands with a low 11.3/9.8 ratio is similar to that of the ISM silicate absorption feature. Such 10 micron features are indicative of small, amorphous silicate grains, i.e. relatively “primitive” dust. The emission bands with high 11.3/9.8 ratios can be explained with on average larger grains, and a higher degree of crystallinity, i.e. relatively “processed” dust. Thus, the silicate feature 11.3/9.8 ratio is a measure of the amount of processing that the material has undergone (Bouwman et al. 2001).

$F_{\nu,c} >$, where $F_{\nu,cs}$ is the continuum subtracted spectrum ($F_{\nu} - F_{\nu,c}$) and $\langle F_{\nu,c} \rangle$ is the mean of the continuum. This definition of $F_{\nu,cs}$ preserves the shape of the emission band even if the continuum is not constant. For a constant continuum level it is identical to $F_{\nu}/F_{\nu,c}$.

5. Analysis

5.1. Compositional fits

To derive the composition of the silicate dust causing the 10 micron feature, the observed spectra have been fitted using the most commonly found dust species in circumstellar material that show spectral structure in the 10 micron region (see Fig. 7). These are amorphous and crystalline olivine and pyroxene, and amorphous silica (e.g. Bouwman et al. 2001). Amorphous olivine ($Mg_{2x}Fe_{2(1-x)}SiO_4$, where $0 \lesssim x \lesssim 1$ denotes the magnesium content of the material) is the most commonly found silicate in astrophysical environments. It dominates the 10 micron extinction caused by dust grains in the ISM (Kemper et al. 2004). The 10 micron emission spectrum of small amorphous olivine grains is characterized by a rather broad feature which peaks at $9.8\mu m$. Small amorphous pyroxene grains ($Mg_xFe_{1-x}SiO_3$) show an emission feature very similar to that of amorphous olivine grains, though shifted toward shorter wavelengths. The emission spectra from small crystalline olivine and pyroxene grains show strong, narrow resonances that are observed in for example circumstellar disks (Waters & Waelkens 1998; Bouwman et al. 2001) and comets (Crovisier et al. 1997; Bouwman et al. 2003). From the positions of the resonances in the emission spectra of these objects it is clear that the magnesium rich components dominate the emission (see e.g. Jäger et al. 1998). In our fitting procedure we therefore use crystalline olivine and pyroxene with $x = 1$, i.e. forsterite and enstatite respectively. For the amorphous olivine and pyroxene we use $x = 0.5$.

Studies of interplanetary dust particles (Rietmeijer 1989) have shown that some of these particles contain large inclusions of silica (SiO_2). Also, from laboratory experiments it is suggested that when amorphous silicates are annealed to form forsterite, silica will be formed (see e.g. Fabian et al. 2000). The emission spectrum of silica in the 10 micron region has a distinct spectral signature, with a strong feature peaking at $8.9\mu m$. Therefore, silica is included as one of the possible dust components.

Many of our sources show emission bands at 7.9 , 8.6 , 11.3 and $12.7\mu m$ that are attributed to PAHs. In order to include the PAH emission in our compositional fits, we constructed a simple PAH template. This was done by taking our two highest quality spectra of sources without a silicate feature (HD 97048 and HD 169142), subtracting the continuum emission, and averaging over the two spectra. The resulting PAH emission spectrum was added as a fit component, and is shown in the bottom panel of Fig. 7.

Dust grains in circumstellar environments are most likely aggregates of many different dust species. However, in order to perform an analysis of the abundances of the various components in a large sample of sources, it is not (yet) feasible to do computations for such complex aggregates. If the aggregates are very fluffy, the constituents of which they are composed will interact with the incident radiation as separate entities. Molster et al. (2003) show that indeed a measurement of the infrared spectrum of a relatively large

IDP still displays the spectral structure one would expect from much smaller particles. Therefore, we assume that the emission properties of an aggregated structure can be represented by the sum of the emission properties of the constituents (for a similar approach see e.g. Brucato et al. 1999; Bouwman et al. 2001; Honda et al. 2004).

All dust grains contributing to the $10\mu\text{m}$ region will in principle have their own temperature depending on the grain size and composition as well as on position in the disk. Consequently, the emission function of the dust will be a (weighted) sum over blackbody curves of different temperatures. In order to account for these effects one should use a disk model that self-consistently describes the disk geometry and all relevant radiation processes. This is beyond the scope of the analysis presented here. For state of the art disk models we refer to Dullemond & Dominik (2004). We add that even these sophisticated models still do not account for many relevant processes, including the settling and (turbulent) mixing of grains leading to spatial gradients in the dust properties. Such spatial gradients have been reported by van Boekel et al. (2004a) to exist in Herbig Ae disks. One should also realize that even if such a detailed modeling approach was attempted, the modest wavelength interval provided by the TIMMI2 data would reveal only very limited information on the temperature distribution. The continuum in the 10 micron region is a very smooth, almost linear function of wavelength. We therefore opted to represent the continuum by a single blackbody curve with a temperature, T_c that is characteristic for the dust emission as a whole. Inherent in this approach is that we essentially assume that the temperature of the individual grains is independent of composition and size, and that there are no gradients in grain properties (per unit mass) throughout the disk.

The disk regions that we study are partially optically thick at $10\mu\text{m}$. However, we assume that the disk surface layer from which the observed flux originates is optically thin at this wavelength. This must be the case since we see emission features. The flux emitted by a distribution of dust grains is then given by

$$\mathcal{F}_\nu^{\text{silicate}} \propto B_\nu(T_c) \sum_i w_i \kappa_i, \quad (6)$$

where $B_\nu(T_c)$ denotes the Planck function at the characteristic temperature T_c , κ_i is the mass absorption coefficient of dust component i (see also Fig. 7), and w_i is a weighting factor which is proportional to the total dust mass in component i . The summation is over all dust components. The mass absorption coefficient of each dust species is determined by the size, shape, structure and chemical composition of the dust grains. The total model spectrum $\mathcal{F}_\nu^{\text{model}}$ is then calculated by adding a continuum and PAH contribution to the silicate emission.

5.1.1. Shape of the dust grains

The shape and structure of the dust grains are very important parameters determining the feature shape of the emission spectrum. Usually it is assumed that the grains are homogeneous and spherical so that Mie theory can be applied to calculate the κ_i . Another widely used assumption is that the grains are much smaller than the wavelength of radiation (“Rayleigh limit”) in which case it is mathematically straightforward to adopt a continuous distribution of ellipsoids (CDE Bohren & Huffman 1983; Bouwman et al. 2003). Since micron sized silicate grains are not in the Rayleigh limit at a wavelength of 10 μm , we cannot use CDE calculations to study grain growth. Furthermore, a comparison between calculations of the mass absorption coefficients of small crystalline silicates with measurements shows that we cannot get good agreement using homogeneous spherical particles (see for example Fabian et al. 2001).

Adopting different grain shapes, Min et al. (2003) showed that the absorption properties can be divided in essentially two categories. One category contains the perfect homogeneous spheres; the other all other investigated shapes, including hollow spheres. Shape effects within the second category do exist, but they are small compared to the differences with homogeneous spheres. One could say that the difference between perfect homogeneous particles and those having other shapes is essentially a result of a breaking of perfect symmetry (see also Min et al. 2003). This implies that we have only very limited information on the true (likely irregular) shape of astrophysical dust grains from spectroscopic analysis. However, a practical implication of this result is that one may represent the absorption properties of irregular grains with sufficient accuracy by adopting the average properties of a distribution of shapes other than that of homogeneous spheres. For this purpose, a practical choice is a distribution of hollow spheres (DHS), simply averaging over the volume fraction occupied by the central inclusion, which ranges from 0 to 1. In this shape distribution, the material volume of the particle is kept constant, thus particles with a high value of f will have a large outer radius. This shape distribution has the advantage that it can be applied for all grain sizes using a simple extension of Mie theory. Min et al. (2003) showed that this indeed gives excellent results for small forsterite grains. Therefore, in this work, the mass absorption coefficients of all crystalline grains (forsterite, enstatite) and silica are calculated with a distribution of hollow spheres. For the amorphous olivine and pyroxene particles we use Mie theory since for these species the effects of shape on absorption properties are minor.

The κ_i are calculated using laboratory measurements of the refractive index as a function of wavelength. References for the measurements used for the various dust species are listed in Table 5.

Dust component	Chemical formula	Shape	Reference
Amorphous olivine	$Mg_{2x}Fe_{2-2x}SiO_4$	Homogeneous Spheres	Dorschner et al. 1995
Amorphous pyroxene	$Mg_xFe_{1-x}SiO_3$	Homogeneous Spheres	Dorschner et al. 1995
Crystalline forsterite	Mg_2SiO_4	Irregular (DHS)	Servoin & Piriou 1973
Crystalline enstatite	$MgSiO_3$	Irregular (DHS)	Jäger et al. 1998
Amorphous silica	SiO_2	Irregular (DHS)	Spitzer & Kleinman 1960

Table 5. Characteristics of the various dust components used in the fitting procedure (see section 5.1). The chemical formulae and assumed grain shapes have been indicated in the second and third column. In the fourth column, we give references for the refractive index data used.

5.1.2. Size of the dust grains

The dust grains in circumstellar disks most likely have a rather broad size distribution. In the 10 micron region the observational data are sensitive to the dust grains with a volume equivalent radius up to a few micron in size. Larger grains mainly contribute to the continuum. In order to minimize the number of free parameters in the fitting procedure, we want to sample the size distribution carefully. We find that the variety of spectral shapes can be best covered using only two distinct particle sizes, a ‘small’ particle size with a material volume equivalent sphere radius $r_V = 0.1 \mu m$ and a ‘large’ particle size with $r_V = 1.5 \mu m$ (for a similar approach see Bouwman et al. 2001; Honda et al. 2004). We have extensively checked that the results of the analysis using three, four or five particle sizes with volume equivalent radii ranging up to $3.5 \mu m$ do not change significantly. The size of the large grain component, when using only two particle sizes, has to be chosen with care. When it is too large, the difference in absolute value of the mass absorption coefficients of the small and the large grain component will be too big. If, for example, one adopts for the large grain size $r_V = 2 \mu m$, one would overestimate the abundance of large grains. This is especially so for the large crystalline grains and results in an overestimate of the crystallinity. The differences between the absolute values of the emissivities of a 0.1 and a $2 \mu m$ amorphous grain are not so big. Actually, adopting $2 \mu m$ sized grains is even slightly better for the large amorphous component (see also Bouwman et al. 2001). However, considering both the amorphous and crystalline component, $1.5 \mu m$ is the best choice for the large grains.

5.1.3. Fitting procedure and error analysis

In order to keep the number of free parameters in the model small, only two grain sizes are used for every silicate dust type (as discussed above). We thus have contributions of five silicate species, of PAHs and of a blackbody continuum of which the absolute level

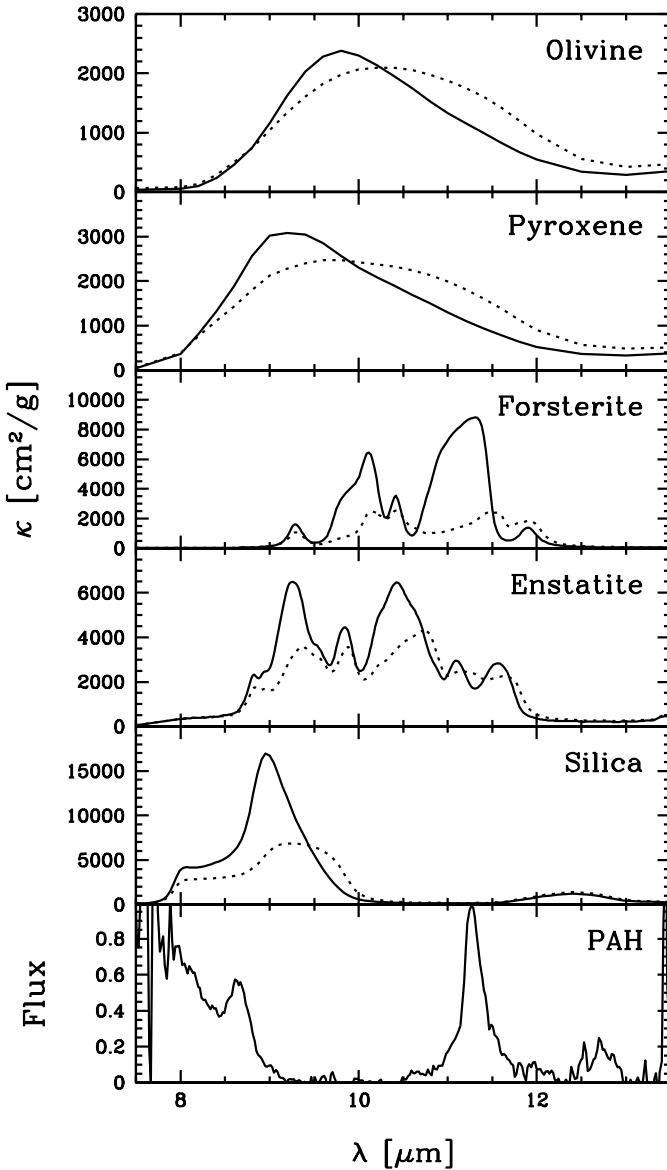


Fig. 7. The mass absorption coefficients of the various templates used in the fitting procedure (upper 5 panels). We use grains with volume equivalent radii of $0.1\text{ }\mu\text{m}$ (solid lines) and $1.5\text{ }\mu\text{m}$ (dotted lines). In the lower panel we show the template used for the PAH emission, which is normalized such that the maximum flux in the 8 to 13 micron region equals unity. For a detailed discussion see section 5.1.

and shape (characteristic temperature) can be varied. The emissivities of the silicates are multiplied by a blackbody spectrum with the same characteristic temperature as the continuum. This results in 13 free parameters. The silicate and PAH templates are shown in Fig. 7.

To fit the spectra we minimize the reduced χ^2 of the entire 10 micron region given by

$$\chi^2 = \frac{1}{N_\lambda - M} \sum_{i=1}^{N_\lambda} \left| \frac{\mathcal{F}_\nu^{\text{model}}(\lambda_i) - \mathcal{F}_\nu^{\text{observed}}(\lambda_i)}{\sigma_i} \right|^2. \quad (7)$$

Here N_λ is the number of wavelength points λ_i , M is the number of fit parameters (in this case $M = 13$) and σ_i is the absolute error on the observed flux at wavelength λ_i . For a given characteristic temperature T_c we can calculate the optimal values for the weights w_i of the individual dust components, using a linear least square fitting procedure.

The measurement errors (σ_i) used in the fitting procedure represent the statistical noise in the spectra. The calibrator spectra all have a very high signal to noise ratio (SNR) and statistical noise of the calibration observations is negligible. The SNR in our Herbig star spectra range from ~ 18 in the faintest source (HD 135344) to approximately 60 in the bright sources (e.g. HD 100546). There are also systematic uncertainties, arising from an imperfect calibration, and the uncertainty in the used spectral templates for the calibrators. Some degree of systematic error is inevitable, since the science target and calibrator cannot be measured at the same time and in the same direction. Since we cannot assess the systematic uncertainties we do not take these into account. We note, however, that agreement between our ground based spectra and high SNR ISO spectra is generally very good. For the faint sources (such as UX Ori), the statistical noise dominates the error budget. For bright sources (e.g. HD 144432) the systematic uncertainties may be important, implying that we underestimate the errors. This will evidently lead to higher χ^2 values in the fit procedure.

The errors on the fit parameters are calculated using a Monte Carlo method. For every spectrum we generate 1000 synthetic spectra, by randomly adding Gaussian noise to the spectrum with a distribution of width σ_i at each wavelength point. This yields 1000 spectra that are all consistent with our data. On each of these, we perform the exact same compositional fit procedure, yielding (slightly) different values of the fit parameters. From the resulting distribution of all fit parameters, we calculate the mean (which will be our 'best fit' value) and standard deviation. Besides its simplicity, this method has the advantage that degeneracies between fit parameters automatically show up as large errors in these parameters.

5.2. Results

Fig. 4 shows the observed spectra together with the best fit model spectra. For comparison we also fit the interstellar extinction as observed towards the galactic center (Kemper et al. 2004). The resulting values of the fit parameters are summarized in Table 6. The overall quality of the model fits is very good and we thus conclude that the diversity of the shapes of the observed spectra are well covered by the choice of the spectral templates. We notice that in some sources the model fits show slightly more spectral structure between 9 and $11\mu\text{m}$ than the observed spectra. This could be caused by the choice of the shape distribution of the dust grains, which may be too simple to represent the spectral details of realistic particles. We also notice that in, for example, HD 179218 we

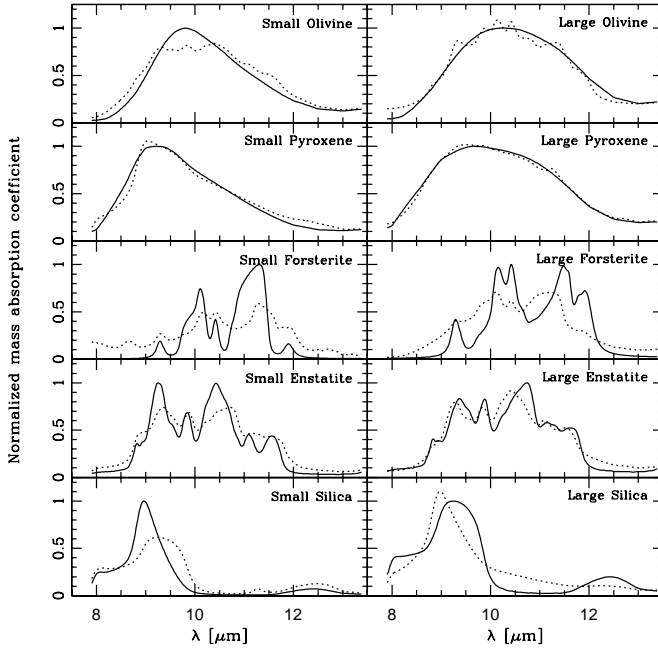


Fig. 8. The templates used in the fitting procedure (solid curves) together with the resulting best fits using all other templates (dotted curves). The spectra are all normalized such that the maximum value of the template equals unity. In the left column we show the templates for the small grains ($0.1 \mu\text{m}$), in the right column those of the large grains ($1.5 \mu\text{m}$).

cannot accurately reproduce the detailed shape of the spectrum. Especially the feature around $11.3 \mu\text{m}$ is less sharply peaked in the observed spectrum than in the model fit. This effect can also be seen in other sources, albeit in a more modest form, and could be caused by a missing dust component or by the choice of the shape distribution.

As an objective measure for the goodness of fit, the reduced χ^2 of every fit is listed in Table 6. For a good fit this parameter should be close to unity. The likely reason that we have relatively high values of χ^2 for about half of the sources is that we do not take into account the uncertainties on the κ_i . These are mainly caused by uncertainties in the shape, structure and size of the grains, and in the laboratory measurements of the wavelength dependent refractive indices.

To test whether we have degeneracies between the various templates used in the fitting procedure we tried to fit each of the silicate templates using a linear combination of all other templates. The results are shown in Fig. 8 where we plot the mass absorption coefficients together with the best fit using the other templates (here the mass absorption coefficients have been normalized such that the maximum value equals unity). The figure shows that almost all of the templates used have a unique spectral structure that cannot be reproduced by the other templates. Only the emission from large pyroxene grains can

Table 6. The best fit values of the parameters in our compositional fits. The abundances of small ($0.1\mu\text{m}$) and large ($1.5\mu\text{m}$) grains of the various dust species are given as fractions of the total dust mass, *excluding* the dust responsible for the continuum emission. If a species was not found, or unconstrained by the spectra, this is indicated by a - symbol. The PAH and continuum flux contributions (the last two columns) are listed as percentages of the total integrated flux over the $10\mu\text{m}$ region, contained in these components. These are measures for the relative flux contributions, but cannot be interpreted as relative dust masses.

#	Star	χ^2	T_c [K]	Olivine		Pyroxene		Forsterite		Enstatite		Silica		PAH	Cont.	
				Small	Large	Small	Large	Small	Large	Small	Large	Small	Large			
0	Gal. Center	66.8	-	$85.8^{+0.1}_{-0.1}$	-	$12.5^{+0.1}_{-0.1}$	-	$0.6^{+0.0}_{-0.0}$	-	-	-	-	$1.0^{+0.0}_{-0.0}$	$0.5^{+0.0}_{-0.0}$	-	
1	AB Aur	2.5	464^{+6}_{-4}	$49.5^{+2.2}_{-2.4}$	$47.2^{+2.5}_{-2.6}$	-	-	$0.6^{+0.2}_{-0.2}$	$2.7^{+0.7}_{-0.7}$	-	-	-	-	$1.9^{+0.1}_{-0.2}$	$53.1^{+0.5}_{-0.4}$	
2	UX Ori	0.7	677^{+29}_{-38}	$63.6^{+4.9}_{-4.5}$	$30.7^{+6.0}_{-7.9}$	-	-	$2.0^{+5.8}_{-1.8}$	$1.2^{+0.4}_{-0.4}$	$0.3^{+0.9}_{-0.3}$	$0.6^{+0.6}_{-0.4}$	$1.1^{+1.2}_{-0.8}$	-	$0.6^{+0.4}_{-0.4}$	$0.1^{+0.3}_{-0.1}$	$45.2^{+1.3}_{-1.4}$
3	HD 36112	1.7	669^{+19}_{-21}	$50.5^{+1.8}_{-1.7}$	$22.4^{+3.2}_{-3.1}$	-	-	$22.2^{+1.8}_{-1.8}$	$2.9^{+0.1}_{-0.1}$	$0.0^{+0.1}_{-0.0}$	$1.8^{+0.2}_{-0.2}$	$0.2^{+0.4}_{-0.2}$	-	-	$0.1^{+0.1}_{-0.1}$	$33.9^{+0.4}_{-0.5}$
4	HK Ori	0.4	516^{+12}_{-11}	$7.1^{+7.6}_{-5.4}$	$0.9^{+16.3}_{-0.9}$	$13.7^{+7.2}_{-7.9}$	$75.3^{+9.9}_{-13.3}$	$0.7^{+1.0}_{-0.6}$	$1.4^{+2.7}_{-1.3}$	$0.1^{+1.0}_{-0.1}$	$0.1^{+1.6}_{-0.1}$	-	-	$0.8^{+1.6}_{-0.8}$	$2.5^{+0.4}_{-0.4}$	$68.5^{+1.4}_{-1.3}$
5	HD 245185	0.6	337^{+7}_{-9}	$28.5^{+3.5}_{-3.5}$	$57.4^{+7.5}_{-8.8}$	$0.1^{+2.5}_{-0.1}$	$12.2^{+6.5}_{-5.9}$	$0.2^{+0.3}_{-0.2}$	$0.7^{+0.9}_{-0.6}$	$0.0^{+0.3}_{-0.0}$	$0.0^{+0.7}_{-0.0}$	-	-	$0.9^{+0.5}_{-0.5}$	$1.1^{+0.2}_{-0.3}$	$50.6^{+1.1}_{-1.1}$
6	V380 Ori	1.8	481^{+9}_{-1}	-	$0.8^{+6.5}_{-0.8}$	-	-	$74.6^{+2.9}_{-5.0}$	$2.2^{+0.6}_{-0.5}$	$10.8^{+1.5}_{-1.4}$	-	$10.8^{+1.8}_{-1.7}$	$0.8^{+0.3}_{-0.3}$	$0.0^{+0.4}_{-0.0}$	$0.7^{+0.1}_{-0.1}$	$84.9^{+0.5}_{-0.4}$
7	HD 37357	0.5	508^{+22}_{-25}	$3.9^{+5.9}_{-3.4}$	$39.4^{+11.9}_{-14.8}$	$0.1^{+3.6}_{-0.1}$	$46.0^{+10.4}_{-9.9}$	$2.7^{+0.5}_{-0.6}$	$2.2^{+1.8}_{-1.5}$	$0.9^{+0.9}_{-0.7}$	$1.3^{+1.8}_{-1.1}$	$0.0^{+0.2}_{-0.0}$	$3.5^{+0.8}_{-0.8}$	$0.1^{+0.3}_{-0.1}$	$47.5^{+1.6}_{-1.5}$	
8	HD 37806	1.8	525^{+7}_{-6}	-	$59.8^{+4.6}_{-5.7}$	-	-	$0.8^{+5.2}_{-0.8}$	$6.2^{+0.9}_{-0.8}$	$3.5^{+1.9}_{-1.8}$	$0.2^{+0.9}_{-0.2}$	$20.9^{+2.7}_{-2.6}$	$5.0^{+0.4}_{-0.4}$	$3.5^{+0.8}_{-0.8}$	$1.8^{+0.2}_{-0.2}$	$73.7^{+1.0}_{-0.9}$
9	HD 95881	3.7	429^{+2}_{-9}	-	-	-	-	$79.7^{+4.0}_{-2.7}$	$0.7^{+0.5}_{-0.5}$	$4.7^{+1.6}_{-1.9}$	$0.0^{+0.8}_{-0.0}$	$11.3^{+1.7}_{-2.4}$	$3.0^{+0.3}_{-0.3}$	$0.5^{+0.9}_{-0.5}$	$3.0^{+0.2}_{-0.1}$	$84.2^{+0.4}_{-0.7}$
10	HD 97048	1.4	303^{+7}_{-3}	-	-	-	-	-	-	-	-	-	-	$14.1^{+0.2}_{-0.2}$	$83.1^{+0.6}_{-0.4}$	
11	HD 100453	2.1	429^{+1}_{-9}	-	-	-	-	-	-	-	-	-	-	$4.4^{+0.1}_{-0.1}$	$93.5^{+0.2}_{-0.4}$	
12	HD 100546	5.6	261^{+9}_{-1}	$2.5^{+1.1}_{-1.6}$	$78.5^{+1.3}_{-1.2}$	-	-	$0.0^{+0.7}_{-0.0}$	$6.2^{+0.8}_{-0.2}$	$0.1^{+0.4}_{-0.1}$	-	$5.7^{+0.5}_{-0.4}$	$0.2^{+0.1}_{-0.1}$	$6.7^{+0.3}_{-0.6}$	$3.7^{+0.1}_{-0.6}$	$55.3^{+2.9}_{-0.6}$
13	HD 101412	0.5	425^{+6}_{-5}	-	$0.3^{+9.1}_{-0.3}$	$0.2^{+4.3}_{-0.2}$	$75.2^{+5.4}_{-7.0}$	$0.7^{+1.2}_{-0.6}$	$3.4^{+3.1}_{-2.5}$	$0.1^{+1.2}_{-0.1}$	$16.8^{+3.9}_{-3.4}$	$3.2^{+0.6}_{-0.6}$	$0.1^{+1.2}_{-0.1}$	$2.0^{+0.2}_{-0.2}$	$80.2^{+1.1}_{-0.9}$	
14	HD 104237	3.9	446^{+4}_{-6}	-	-	-	-	$77.7^{+1.6}_{-1.3}$	$5.9^{+0.4}_{-0.6}$	-	-	$11.8^{+1.0}_{-1.2}$	$1.7^{+0.2}_{-0.1}$	$2.9^{+0.4}_{-0.4}$	$1.4^{+0.2}_{-0.1}$	$63.4^{+0.6}_{-0.9}$
15	HD 135344	0.8	680^{+18}_{-14}	-	-	-	-	-	-	-	-	-	-	$4.9^{+0.3}_{-0.3}$	$90.3^{+1.0}_{-1.0}$	
16	HD 139614	0.6	277^{+4}_{-7}	$16.0^{+6.2}_{-6.5}$	$47.0^{+11.2}_{-16.7}$	-	-	$29.7^{+13.8}_{-9.8}$	$2.4^{+0.9}_{-0.8}$	$0.7^{+1.7}_{-0.6}$	$0.0^{+0.7}_{-0.0}$	$4.1^{+2.3}_{-2.1}$	-	$0.1^{+0.7}_{-0.1}$	$2.2^{+0.3}_{-0.3}$	$75.9^{+1.3}_{-1.6}$
17	HD 142666	1.6	396^{+4}_{-6}	$42.8^{+2.9}_{-2.7}$	$9.7^{+5.0}_{-6.5}$	-	-	$43.5^{+3.9}_{-2.9}$	$1.1^{+0.3}_{-0.3}$	$2.3^{+0.8}_{-0.8}$	$0.0^{+0.3}_{-0.0}$	$0.6^{+0.8}_{-0.5}$	-	-	$1.7^{+0.2}_{-0.1}$	$66.8^{+0.5}_{-0.5}$
18	HD 142527	11.1	523^{+8}_{-3}	-	$0.0^{+0.8}_{-0.0}$	-	-	$73.2^{+0.7}_{-1.0}$	$8.6^{+0.4}_{-0.2}$	-	$0.6^{+0.2}_{-0.2}$	$14.2^{+0.8}_{-0.6}$	$2.4^{+0.1}_{-0.1}$	$1.0^{+0.2}_{-0.3}$	$3.1^{+0.1}_{-0.2}$	$58.8^{+0.7}_{-0.3}$
19	HD 144432	3.0	401^{+10}_{-1}	$52.7^{+0.7}_{-0.7}$	$0.0^{+1.1}_{-0.0}$	-	-	$42.3^{+0.7}_{-0.8}$	$1.9^{+0.1}_{-0.1}$	$0.7^{+0.3}_{-0.3}$	$0.7^{+0.2}_{-0.2}$	$0.9^{+0.3}_{-0.3}$	-	$0.6^{+0.1}_{-0.1}$	$0.5^{+0.1}_{-0.1}$	$39.7^{+0.5}_{-0.3}$
20	HD 144668	9.6	517^{+3}_{-7}	-	$56.9^{+6.8}_{-13.2}$	-	-	$12.0^{+12.4}_{-6.1}$	$7.0^{+0.3}_{-0.3}$	$6.3^{+0.9}_{-0.8}$	$0.0^{+0.3}_{-0.0}$	$12.1^{+0.9}_{-0.8}$	$1.5^{+0.2}_{-0.3}$	$4.2^{+0.3}_{-0.3}$	$1.2^{+0.1}_{-0.1}$	$85.3^{+0.2}_{-0.3}$
21	HD 150193	5.1	410^{+0}_{-10}	-	$0.7^{+1.1}_{-0.6}$	-	-	$82.1^{+0.7}_{-0.8}$	$3.3^{+0.1}_{-0.1}$	$4.1^{+0.3}_{-0.3}$	$0.2^{+0.2}_{-0.2}$	$3.7^{+0.3}_{-0.4}$	-	$5.8^{+0.1}_{-0.1}$	$0.2^{+0.1}_{-0.1}$	$39.7^{+0.2}_{-0.3}$
22	HD 163296	10.7	461^{+9}_{-1}	$15.3^{+0.7}_{-1.4}$	$29.8^{+3.8}_{-1.4}$	-	-	$42.2^{+0.8}_{-2.1}$	$3.1^{+0.1}_{-0.1}$	$1.3^{+0.3}_{-0.3}$	$0.2^{+0.1}_{-0.1}$	$4.0^{+0.3}_{-0.3}$	-	$4.1^{+0.1}_{-0.1}$	$1.1^{+0.1}_{-0.1}$	$49.6^{+0.2}_{-0.2}$
23	HD 169142	0.9	348^{+4}_{-8}	-	-	-	-	-	-	-	-	-	-	$16.1^{+0.2}_{-0.2}$	$82.0^{+0.4}_{-0.5}$	
24	HD 179218	11.8	350^{+0}_{-14}	-	$11.3^{+2.6}_{-2.6}$	-	-	$58.7^{+2.1}_{-2.0}$	-	$3.5^{+0.6}_{-0.7}$	$6.2^{+0.4}_{-0.4}$	$18.3^{+0.8}_{-0.7}$	$2.0^{+0.1}_{-0.1}$	-	$4.4^{+0.1}_{-0.1}$	$64.8^{+0.2}_{-0.2}$

be reproduced reasonably well by the other templates, although significant differences still exist (e.g. the $11.3\,\mu\text{m}$ feature that is present in the fit to the large pyroxene opacity in Fig. 8). The fit consists of 52% large olivine grains, 43% small pyroxene grains and only 5% of crystalline silicates. This could result in a slight change in the mass fraction of large grains when this template is not used. The crystalline fraction would not be affected significantly. Because the small pyroxene grains are needed in order to reproduce the short wavelength side of some of the spectra, we chose to include also the large pyroxene grains for consistency. The presence of large pyroxene grains can be firmly established only in the highest SNR spectra.

There are a few points one has to keep in mind when interpreting the results of the analysis presented above.

- Since we consider only the 10 micron region of the infrared spectrum our data are sensitive only to grains with a temperature of $\sim 200\,\text{K}$ or more. This limits our study to the inner disk regions (i.e. $\lesssim 10\text{-}20\,\text{AU}$).
- Because of the same limitation of the spectral range our data are only sensitive to relatively modest sized grains. In order for the emission to show an observable spectral signature, the dust grains have to be small compared to the wavelength of radiation. $10\,\mu\text{m}$ measurements are sensitive to grains with a volume equivalent radius $r_V \lesssim 3\,\mu\text{m}$.
- The disk regions that we study are partially optically thick at $10\,\mu\text{m}$. This means that we cannot see deep into the disk. We only observe the surface layer.
- Due to the limited spatial resolution of our observations, we observe the integrated spectra of the entire inner disk surface. The observed flux is therefore an average over distance to the star and thus over temperature. Also, we know from spatially resolved observations of the innermost part of a few disks that the mineralogy is not constant as a function of distance to the star (van Boekel et al. 2004a). Close to the star we have higher temperatures and densities which trigger both crystallization and grain growth. The derived parameters therefore represent an average, characteristic temperature and an average dust composition.

5.3. Observed trends in the fits

We will now discuss the trends and correlations observed in the derived fit parameters.

In Fig. 9 we visualize the grain growth and crystallinity, as implied by our compositional fits. Horizontally we plot the mass in large ($1.5\,\mu\text{m}$) grains, as a fraction of the total dust mass, *excluding the dust responsible for the continuum component, and the PAHs*. Vertically, we likewise plot the mass fraction contained in crystalline silicates in small and large grains, which is also referred to as the *crystallinity* of the material.

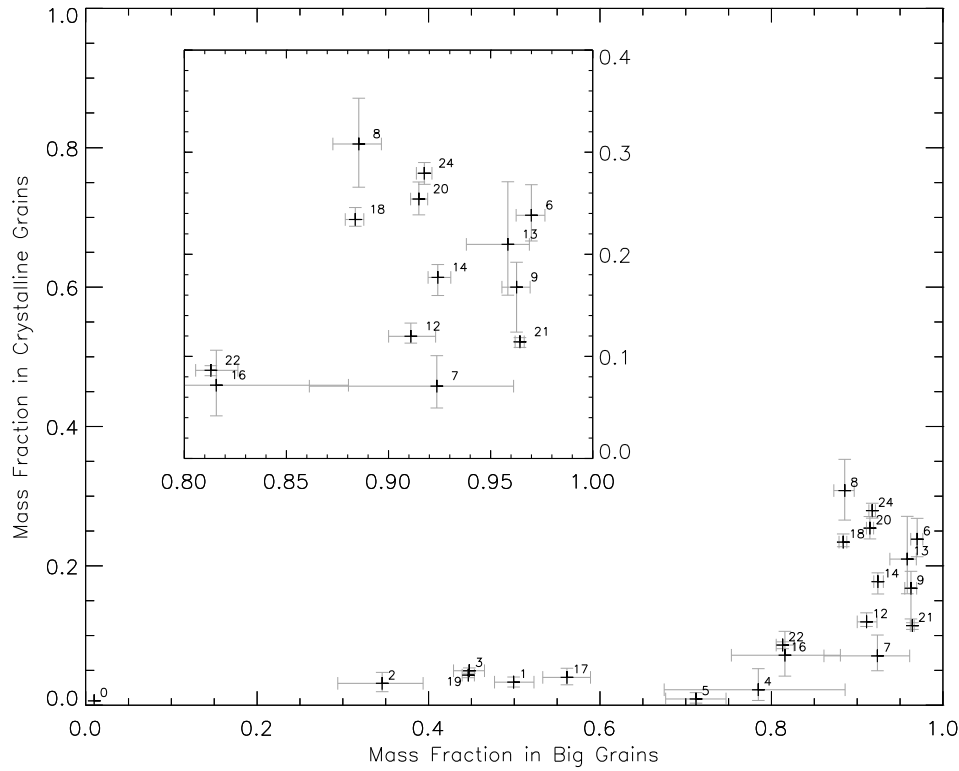


Fig. 9. The relation between grain size and crystallinity found in our spectral fits. Vertically, we plot the mass fraction of crystalline grains (forsterite and enstatite). Horizontally, the mass fraction of large ($1.5 \mu\text{m}$) grains is plotted. Since group Ib sources do not display a silicate feature, they are not shown here. For a discussion see sections 5.3 and 6.

Upon inspection of the figure it is clear that all disks show signs of substantial removal of small grains. There are *no* sources with a mass fraction in large grains below 30%. This infers that none of the sources in our sample contains truly “pristine” dust. All sources have an appreciable amount of large grains at their disk surface, compared to ISM conditions. In addition, all sources have a crystallinity that is higher than the value we derive for the ISM ($\sim 0.6\%$; Kemper et al. 2004 derive an even more stringent upper limit of 0.4%).

The derived mass fraction in large grains ranges from $\approx 30\%$ to $\approx 100\%$, with most sources at high values. *All sources exhibiting a high degree of crystallinity have a high mass fraction in large grains.* There are *no* highly crystalline sources (crystallinity above 10%) with less than 85% of the dust mass in large grains.

There are no sources with a mass fraction of crystalline material above 35% (see also Table 6). It should be kept in mind that the silicate emission we see likely originates in the surface layer of the disk. Van Boekel et al. (2003) argue that the disks are well mixed in the vertical direction, and that therefore the observed silicate emission should

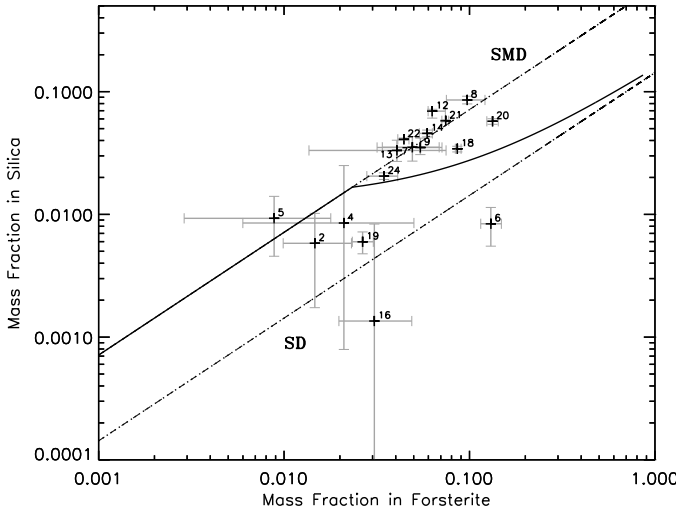


Fig. 10. The fraction of the dust mass contained in silica grains vs. the mass fraction contained in forsterite grains. Following Bouwman et al. (2001) we also plot the theoretical annealing behavior of two different amorphous magnesium silicates, smectite dehydroxylate (SMD; $\text{Mg}_6\text{Si}_8\text{O}_{22}$; upper dashed line) and serpentine dehydroxylate (SD; $\text{Mg}_3\text{Si}_2\text{O}_7$; lower dashed line). The solid line represents the expected annealing behavior of a mixture of these two silicates, consisting of 4% SMD and 96% SD, which was found by Bouwman et al. (2001) to give the best fit to their data. Our data are in better agreement with a pure SMD initial composition.

be representative of the whole micron and sub-micron sized dust population of the disk. We point out that in this work, “crystallization” refers to the process of crystallizing the material (by whatever means), spreading it over a significant part of the disk region seen at $10\text{ }\mu\text{m}$, *and* bringing it up to the disk surface where we can see it spectroscopically. In a scenario where the crystalline silicates are produced by thermal annealing in the innermost disk regions, and transported outward by radial mixing, the degree of crystallization is therefore a measure of the degree of mixing in the disk rather than the actual process of annealing, which is effectively instantaneous at the inner disk edge.

In Fig. 10 we plot the mass fraction of dust contained in forsterite versus that contained in silica grains. It is clear that these mass fractions are correlated. Experiments show that when forsterite is created by annealing of an amorphous silicate, silica is formed as a by-product (Rietmeijer et al. 1986; Hallenbeck & Nuth 1997; Fabian et al. 2000). The amount of silica that is created when forming a certain amount of forsterite depends on the type of amorphous silicate one starts out with. As already suggested by Bouwman et al. (2001), we can try to constrain the composition of the amorphous material by measuring the ratio of forsterite over silica. In the figure we also plot the expected annealing behaviour of smectite dehydroxylate (SMD; $\text{Mg}_6\text{Si}_8\text{O}_{22}$) and serpentine dehydroxylate (SD; $\text{Mg}_3\text{Si}_2\text{O}_7$). In low temperature condensation experiments, these are the only mag-

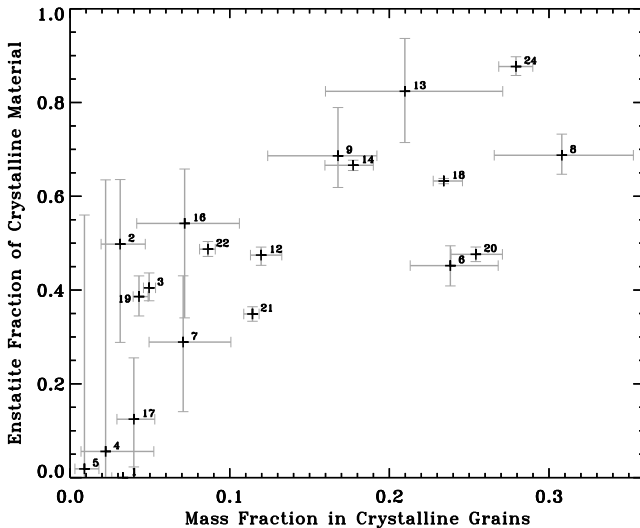


Fig. 11. The mass fraction of crystalline material contained in enstatite vs. the total mass fraction of crystalline material. A value of 0 on the vertical axis indicates that all the crystalline silicates present in the disk are in the form of forsterite, while a value of 1 means all crystalline silicates are in the form of enstatite.

nesium silicates that are formed (Rietmeijer et al. 1999). Whereas Bouwman et al. (2001) found that a mixture of 4% of SMD and 96% of SD yielded the best fit to their data, our results seem to favour an initial composition of pure SMD. Possibly, the discrepancy between the results found by Bouwman et al. (2001) and the results found here is connected to the differences in the dust components used to fit the $10\mu\text{m}$ spectra. Notably, Bouwman et al. (2001) do not include large silica and forsterite particles.

In Fig. 11 we show the mass fraction of crystalline material contained in enstatite versus the total mass fraction of crystalline material. There is a correlation between the fraction of the total mass contained in crystalline silicates and the composition of these crystalline silicates. In general, for sources with a high degree of crystallinity most crystals are in the form of enstatite, while for the sources with a low crystallinity, forsterite is the dominant crystalline species. We will discuss this further in section 6.3.

The amount of growth that the crystalline material has experienced is compared to the growth in the amorphous component in Fig. 12. If the amorphous grains are large, also the crystalline grains are large, though the correlation is not tight. In all sources in which the amorphous component has more than 85% large grains, also the crystalline component is dominated by large grains. The sources that have less than 85% large grains in the amorphous component all have a low crystallinity (see Fig. 9). Therefore, the ratio of large and small crystals is poorly constrained in these sources, which is reflected in the large errorbars.

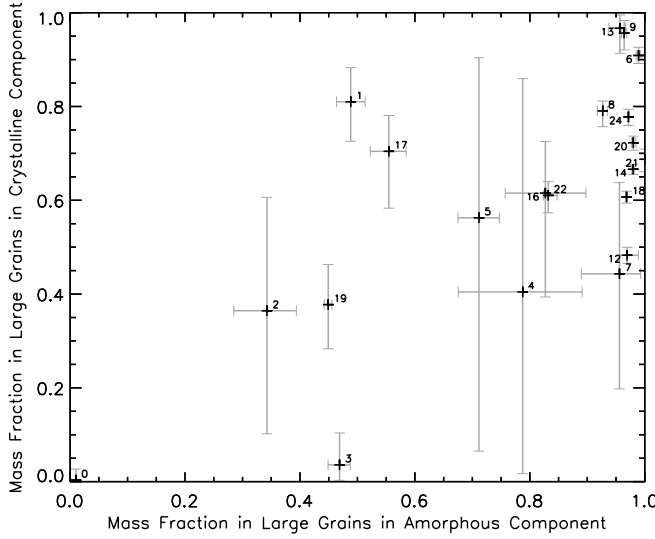


Fig. 12. The mass fraction of large grains in the crystalline grain population vs. the mass fraction of large grains in the amorphous component. When the average size of the amorphous grains is large, the majority of the crystalline material resides in large grains as well.

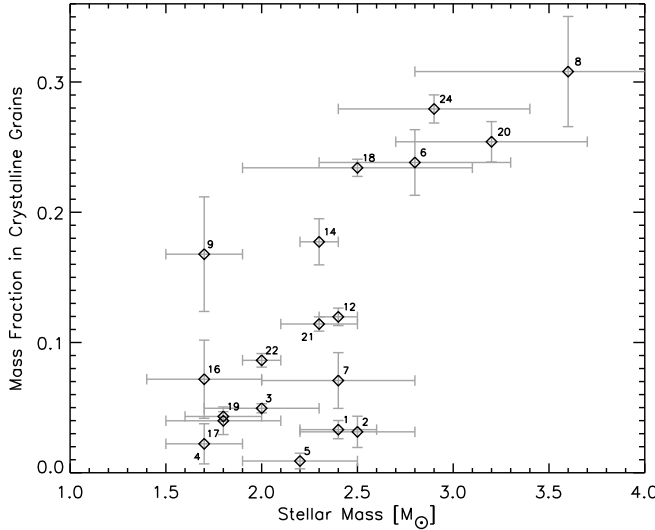


Fig. 13. The mass fraction of dust in crystalline grains vs. the stellar mass. Higher mass stars show an on average higher fraction of crystalline grains than do lower mass stars.

The fraction of crystalline silicates is correlated with the mass and luminosity of the central star. This is visualized in Fig. 13. The higher mass (higher luminosity) stars have an on average higher crystallinity than the lower mass (lower luminosity) stars. This correlation will be discussed in section 6.3.

All stars with a stellar mass above about $2.5 M_{\odot}$ ($L > 60 L_{\odot}$) have a high fraction ($\gtrsim 85\%$) of large grains (Fig. 14). Possibly, conditions in the disks around more massive

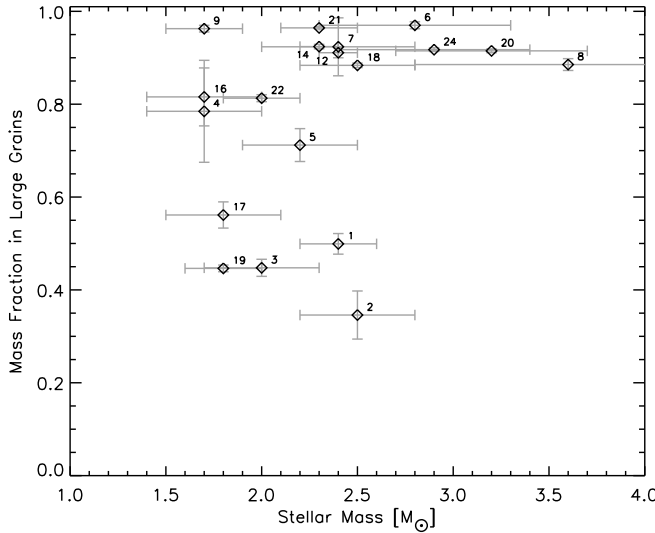


Fig. 14. The mass fraction of dust residing in large grains vs. the stellar mass. All stars with a mass $M \gtrsim 2.5 M_{\odot}$ have a mass fraction of large grains above 85 %.

stars are more favourable for growth than they are in the disks around lower mass stars. An alternative explanation for the observed trend is that the disks around the more massive stars, which are all relatively young (Fig. 2), are more turbulent than those around the less massive, older stars. As a consequence the mixing in the young disks will be more efficient. While in the older stars the large grains decouple from the gas and settle to the midplane (and therefore will not be detected in the 10 micron spectrum anymore), in the young stars, larger grains may still reach the disk surface and cause the observed average grain size to be higher.

6. Discussion

We now discuss our fit results in terms of the processes that are responsible for the dust evolution. We will first briefly outline the expected conditions that prevailed during the active disk phase (section 6.1), i.e. the phase prior to the passive disk phase. For a comprehensive review of active disks, see e.g. Calvet et al. (2000). The disks of all stars in our sample are in the passive disk phase. The characteristics of this phase are discussed in section 6.2. In section 6.3 we summarize the constraints put on dust processing by this work and previous studies. Lastly, in section 6.4 we sketch a scenario that is consistent with the current knowledge of dust processing and disk evolution.

6.1. The active disk phase

The accretion of matter onto a forming proto-star is believed to be initially spherically symmetric. At some point, as the proto-star contracts, conservation of angular momentum inhibits further spherical accretion. The accretion process then proceeds through a disk,

and is accompanied by a bi-polar outflow. The fact that material is radially transported through the disk implies that the disk has viscosity, which is in turn coupled to turbulence.

During this so-called *active disk phase*, gravitational energy of the accreting material is dissipated in the disk, thereby heating it. Accretion rates in the active phase may reach values up to $10^{-5} M_{\odot} \text{yr}^{-1}$ (Calvet et al. 2000). Close to the central star the main energy source of the disk is accretion luminosity, whereas at larger radii irradiation by the star and hot inner disk regions is expected to be the main heating source of the disk material.

The dust in the disk consists mainly of silicates (studied in this work), and carbon. The dust does not contribute significantly to the disk mass in this phase of the disk evolution (the gas over dust ratio is on the order of 10^2 by mass). However, the thermal radiation emitted by the dust is the dominant cooling process in the disk. In the outer disk regions where the main energy source is irradiation, the dust governs the heating of the disk as well. Therefore, the dust properties determine the disk temperature, except in the innermost disk region where the heating is dominated by viscous dissipation of gravitational energy of the accreting material. The gas, heated by the dust, provides the pressure support of the disk.

The densities in the disk are high, especially near the disk mid-plane, and one may expect coagulation of small dust grains into larger aggregates to occur. Already after $\sim 10^4$ yr of dynamical disk evolution the average mass of a grain can increase by a factor 10^1 to 10^2 , and close to the disk midplane the grains may reach sizes of at least a few times $10 \mu\text{m}$ up to millimeters (Suttner & Yorke 2001). Close to the central star the temperatures in the disk can reach values in excess of 1000 K. At this temperature the (initially mostly amorphous) silicates are annealed, to form crystalline silicates. Yet closer to the star, temperatures reach values of about 1500 K, and crystalline silicates may form by gas phase condensation of evaporated material.

In some of the stars in our sample, the crystalline silicates appear so prominent that it is unlikely that their emission arises from the innermost disk region only; the abundance of crystalline silicates must be high in a relatively large part of the region of the disk responsible for the $10 \mu\text{m}$ emission (the innermost 10-20 AU of the disk). There are in essence two possible ways to get crystalline material at ~ 10 AU distance from the star: (1) thermal processing in the hot inner disk and subsequent radial transport of this material outward, and (2) local production of crystalline material at large distance from the star in transient heating events caused by shocks (e.g. Harker & Desch 2002) or lightning (e.g. Pilipp et al. 1998; Desch & Cuzzi 2000). During the active disk phase the accretion rate in the viscous disk is high and the disk will be turbulent. This is expected to enable radial mixing of material (Bockelée-Morvan et al. 2002; Gail 2004).

6.2. The passive disk phase

When the supply of fresh material from the maternal cloud has exhausted, further accretion onto the star proceeds only on a very low level (order $10^{-8} M_{\odot} \text{yr}^{-1}$). Under these conditions the energy production by viscous dissipation can be fully neglected. Throughout the disk the temperature of the material is determined by absorption of stellar radiation; this is referred to as the *passive disk phase*. The stars that we study are in this evolutionary phase. In the observed SEDs of sources in the passive disk phase, the infrared excess typically becomes noticeable above the photospheric emission at a wavelength of about $1 \mu\text{m}$. The excess emission in the near-infrared indicates that the inner radius of the disk is determined by the evaporation temperature of silicates (at about 1500 K). At wavelengths longward of $2 \mu\text{m}$ the infrared emission from a gas rich disk completely dominates the SED.

The formation of planets and planetesimals is thought to occur during the passive disk phase. As the disk dissipates on a timescale of 10^7 yr , the infrared excess fades. The inner disk regions become devoid of gas and dust first. When the system has evolved into the *debris disk phase* (e.g. β Pictoris, Aumann 1984; Smith & Terrile 1984) excess emission can be seen above the stellar photospheric emission only at wavelengths above $\sim 10 \mu\text{m}$.

6.2.1. The era of crystallization

During the passive disk phase there is a region in the inner disk where the temperature is above 1000 K, and therefore the silicates will be crystallized. As there is no significant accretion luminosity, this region will be smaller than in the active disk phase. It is unclear whether the disk will be turbulent enough for significant radial mixing to take place during the passive phase. Also the proposed mechanisms for local production of crystalline silicates in the outer disk regions are more efficient in the active disk phase. Theoretically therefore, the active disk phase is the preferred era for the crystallization of the dust. Nonetheless it has, from an observational point of view, been suggested that the crystallinity of HAe disks gradually evolves from low to high values during the passive phase (Grady et al. 2000).

6.3. New constraints on dust processing

We first briefly repeat the results that follow directly from our spectral modeling:

1. All disks have already substantial removal of the smallest grains (in our fits represented by the $0.1 \mu\text{m}$ grains). The mass fraction of large (in our fits $1.5 \mu\text{m}$) grains ranges from about 35 to almost 100 percent.

2. The crystallinity ranges from about 5 to 30 percent. Disks with a high crystallinity are always dominated by large grains.
3. Vice versa, disks with more than 85 percent large grains show a crystallinity above 10 percent; disks with less than 85 percent large grains show a crystallinity below 10 percent.
4. Large crystals are found when large amorphous grains are abundant. We do not find disks in which the bulk of the grains is large, and the crystalline silicates are small.
5. In disks with a crystallinity below 15 percent, more than 45 percent of the crystalline silicates consist of forsterite. Above 15 percent crystallinity, more than 45 percent of the crystalline silicates consist of enstatite.

When the stellar parameters of our sample stars (see Table 1) are taken into account, several additional conclusions can be drawn:

6. The disks with the highest degree of crystalline material (between 20 and 30 percent) all belong to stars with a mass above $2.5 M_{\odot}$, and a luminosity above $60 L_{\odot}$.
7. Below a crystallinity of 20 percent, there does not appear to be a correlation between stellar parameters (mass, luminosity, age) and crystallinity. Separate studies of the 10 micron spectra of T Tauri stars (Przygoda et al. 2003; Honda, private communication) indicate that the crystallinities of T Tauri star disks are similar to those observed in the disks of those HAe stars in our sample that have $M \lesssim 2.5 M_{\odot}$ (i.e. $\lesssim 10$ percent). We note that a small subset of the T Tauri star disks shows a significantly higher crystallinity, deviating from the general trend (Honda et al. 2003).
8. The stars in our sample with masses below $2.5 M_{\odot}$ have ages ranging from 2×10^6 to $\sim 10^7$ yr (see Fig. 2). If we consider only this subgroup, we find no relation between the stellar age and the disk crystallinity.
9. The stars that lack a 10 micron silicate emission band (HD 97048, HD 100453, HD 135344 and HD 169142) tend to be old, with ages of 5-10 Myr.

A number of previous studies have been concerned with the crystalline silicates in HAe star disks. Here we briefly recall some of the results that are of relevance for this study:

10. Recent observations using the $10 \mu\text{m}$ instrument MIDI (Leinert et al. 2003) on the VLT Interferometer (Glindemann et al. 2003) have enabled the extraction of the spectra of the innermost ~ 2 AU of three HAe stars (van Boekel et al. 2004a), showing that:
 - HD 144432 has virtually all its crystals in the inner 2 AU.
 - HD 163296 has a flatter crystallinity "gradient" and has a higher overall crystallinity than HD 144432.

- HD 142527 has the highest crystallinity of the three stars studied, virtually the entire inner disk is crystallized. Also at radii larger than 2 AU, the abundance of crystalline silicates is relatively high.
- The innermost regions of the disks have experienced more grain growth than the outer disk regions. Small grains are mostly found at larger distance from these stars.

11. ISO observations of HD 179218 and HD 100546 show the presence of cold (100-150 K) crystalline silicates. This implies a substantial crystallinity even at distances between 20 and 40-50 AU (Malfait et al. 1998b; Bouwman et al. 2001, ME01).
12. A $33.5 \mu\text{m}$ forsterite band is tentatively detected in the ISO spectrum of HD 100453 (Vandenbussche et al. 2004).

We will now discuss the implications of the points mentioned above. For clarity, we have labeled each of the implications with the index number(s) of the point(s) that lead to it.

1, 2, 3: The dust in the circumstellar disks coagulates more easily than it crystallizes.

This is likely due to the fact that the circumstances enabling grain growth (i.e. high densities) prevail in a much larger part of the disk than the circumstances needed for crystallization of silicates (i.e. high temperatures). Once a certain level of coagulation is reached, crystallinity becomes a lot more obvious in the upper layers of the disk.

4: This observation is consistent with crystallization occurring as the grains grow: whatever population of grains is present, is crystallized. Most of the crystallization occurs when the average grain size is already large (micron sized).

1, 2, 3, 10, 12: Coagulation is more efficient in the inner disk regions than in the outer disk regions. In the sources that lack a silicate band coagulation must have proceeded furthest. Our relation between grain growth and crystallization (Fig. 9) then implies that these disks must have a substantial fraction of crystalline silicates, certainly above 10 percent and perhaps more than 20 percent. However, we do not find the usual forsterite band at $11.3 \mu\text{m}$ nor the $23.5 \mu\text{m}$ forsterite band. So, also the crystalline silicates must on average be large. Indeed this is what was concluded for HD 100453 (Vandenbussche et al. 2004). Again, it seems that whatever (inner disk) grain population is present, is crystallized.

4: Micron sized crystalline grains are present in the disks. It is hard to produce crystalline grains of these sizes via shock heating. At any rate, our data put severe limits on the efficiency of shock heating, as the shock mechanism must be able to produce sufficiently strong shocks to crystallize micron sized grains.

5: If we consider two possible sources of crystalline silicates, i.e. chemical equilibrium reactions (gas phase condensation and subsequent gas-solid reactions) and thermal annealing, then we can note the following (Gail 2004):

- Enstatite is expected to be the dominant crystalline species formed by chemical equilibrium processes in most of the inner disk, apart from the hottest, innermost region, which is dominated by forsterite.
- Since most likely amorphous olivine is the most abundant species entering the disk from the ISM, forsterite (or better, crystalline olivine) is expected to be the dominant crystalline species formed by thermal annealing.

In disks with a low crystallinity, forsterite is the dominant crystalline species, suggesting that this material is formed by thermal annealing. The high abundance of enstatite observed in the highly crystalline disks indicates that the production of crystalline material has occurred by means of chemical equilibrium processes in these sources.

1, 2, 3, 4, 10: The TIMMI2 and MIDI data taken together are consistent with crystallization starting in the innermost regions. Disks with a high crystallinity in the TIMMI2 data have a substantial fraction of crystalline grains in the 5-10 AU area (or even in the 20-50 AU region, see e.g. the ISO spectra of HD 100546, HD 179218 (Malfait et al. 1998b; Bouwman et al. 2001)), i.e. well outside the regions where thermal annealing and chemical equilibrium processes are expected to be effective.

5, 11: HD 179218 has a high abundance of cold enstatite. In the context of the above reasoning, this enstatite must have been produced either locally in transient heating events, or transported outward from the inner disk to observable cold disk regions. If chemical equilibrium processes are an important means of producing enstatite, the HD 179218 data point to enstatite production in the inner regions and transport to larger distance by radial mixing.

6: Crystallization is more efficient in disks around higher mass, higher luminosity stars.

Several possible explanations for this trend can be identified:

1. during the active phase, the region in which the disk material is sufficiently hot for thermal annealing (and chemical equilibrium processes) to occur is larger in high mass stars, since the energy dissipated in the disk per unit mass accreted material is higher. If this is the dominant effect, our results favour crystallization in the active phase.
2. during the passive phase, when the extent of the region where annealing (and chemical equilibrium processes) can occur is set by irradiation from the central star, the higher luminosity of the more massive stars causes this region to be larger than in the low mass stars. If this is the dominant effect, our results favour crystallization in the passive phase.

3. the disks around more massive, more luminous stars may be more turbulent, both during the active and passive phase. The outward mixing of processed material will then be more efficient in the high mass stars, causing a more prominent appearance of this dust in the spectrum.

It is currently unclear which of the above effects is dominant. The study of young ($\tau < 10^6$ yr), low mass stars may allow to answer this question.

- 8: This observation suggests that whatever caused the observed range of crystallinities in stars with a mass below about $2.5 M_{\odot}$, occurred before 2×10^6 yr. This puts the epoch of crystallization in the active and/or early passive phase.

6.4. Global picture that emerges

The $10 \mu\text{m}$ emission is emitted by the surface layer of the disk at radii below 20 AU from the central star. In the midplane of this region (and presumably even at larger radii), dust coagulation takes place. Vertical mixing ensures that the coagulated, micron-sized grains reach the disk surface layer and become apparent in the spectrum. Growth is most efficient in the innermost disk regions where the densities are highest. Crystallization by means of thermal annealing and chemical equilibrium processes occurs in the hot innermost disk region. In many disks there are significant amounts of crystalline material at larger ($\gtrsim 5$ AU) distances from the star, where thermal annealing and chemical equilibrium processes are ineffective. The combined evidence presented in section 6.3 seems to favour radial transport from the innermost disk regions as the source of these crystals, above local production mechanisms (e.g. shock annealing).

Crystallization is most efficient in the disks surrounding the more massive, more luminous stars ($M \gtrsim 2.5 M_{\odot}$, $L \gtrsim 60 L_{\odot}$). In these disks, the region in which thermal annealing and chemical equilibrium processes can produce crystalline silicates is larger than in the disks surrounding lower mass stars. Additionally, the disks around the more massive stars may be more turbulent, enabling more efficient radial mixing. It is unclear whether the crystallization of the dust in the disks occurs predominantly in the active disk phase, or in the passive phase that follows. Our data do suggest that the disks reach their final crystallinity relatively early in the passive phase ($\tau \lesssim 2$ Myr). Therefore, crystallization happens during the active and/or early passive phase.

7. Conclusions

We have undertaken a large spectroscopic survey of Herbig Ae stars in the $10 \mu\text{m}$ atmospheric window, and have presented new spectra of 23 stars. The correlation between the shape and the strength of the $10 \mu\text{m}$ silicate emission band reported by van Boekel et al. (2003) is reconfirmed with a larger sample. We have performed compositional fits

to the silicate feature using opacities of minerals commonly found in circumstellar disks (amorphous olivine and pyroxene, crystalline olivine and pyroxene, and amorphous silica) and polycyclic aromatic hydrocarbons. For all minerals we have allowed both “small” ($0.1\,\mu\text{m}$) and “large” ($1.5\,\mu\text{m}$) grains in order to study the effects of grain growth. This set of materials is sufficient to reproduce the wide variety of observed spectral shapes.

We find a trend between the mass fraction in large grains and the mass fraction in crystalline grains: *all sources with a high crystallinity have a high mass fraction in large grains*. There are no highly crystalline sources which are dominated by small grains. Most sources have a mass fraction in large grains of more than 80 percent.

We note that there is an important bias in our sample (and probably in most samples of Herbig stars studied in the literature): the more massive sample stars ($\sim 3\,\text{M}_\odot$, “high mass”) are younger than the less massive ($\lesssim 2.5\,\text{M}_\odot$, “low mass”) stars. There are no low mass stars younger than 1 Myr in our sample. In order to establish the disk conditions at the end of the active disk phase, which precedes the passive phase, it is essential that such very young, low mass stars are found and studied. Since these stars may still be enshrouded in circumstellar material, they may have to be selected using infrared data.

We find a trend between the derived crystallinity of the dust and the mass (and luminosity) of the central star: the disks around stars with a mass larger than $2.5\,\text{M}_\odot$ (a luminosity above $60\,\text{L}_\odot$) have a higher crystallinity ($\gtrsim 20\%$) than the less massive, less luminous stars. Within the subset of sources with a stellar mass below $2.5\,\text{M}_\odot$, no correlation between crystallinity and stellar parameters (mass, luminosity, age) is seen. These lower mass stars in our sample are all older than ~ 2 Myr. Since in this subset there is no correlation between age and crystallinity, we conclude that the crystallization of the material predominantly happens in the active or early passive disk phase (before 2 Myr).

The evidence presented in this paper combined with conclusions from other studies seems to favour a scenario in which crystalline silicates are produced in the innermost regions of the disk and transported outwards. Spatially resolved spectra of these disks, as can be obtained using for example the MIDI instrument on the Very Large Telescope Interferometer, will provide crucial information on the radial dependence of the mineralogy of the dust in these disks. In addition, measurements at longer wavelengths can probe colder regions (further out) in the disk which can provide further constraints on the temperature structure and spatial distribution of the dust.

Acknowledgements. This research has made use of the SIMBAD database, operated at CDS, Strasbourg, France. We gratefully acknowledge J. W. Hovenier for thorough reading and valuable comments on an earlier version of the manuscript.

References

Acke, B. & van den Ancker, M. E. 2004, A&A, 426, 151

Acke, B., van den Ancker, M. E., Dullemond, C. P., van Boekel, R., & Waters, L. B. F. M. 2004, A&A, 422, 621

Augereau, J. C., Lagrange, A. M., Mouillet, D., & Ménard, F. 2001, A&A, 365, 78

Aumann, H. H. 1984, BAAS, 16, 483

Bockelée-Morvan, D., Gautier, D., Hersant, F., Huré, J.-M., & Robert, F. 2002, A&A, 384, 1107

Bohren, C. F. & Huffman, D. R. 1983, *Absorption and Scattering of Light by Small Particles* (New York: Wiley)

Bouchet, P., Schmider, F. X., & Manfroid, J. 1991, A&AS, 91, 409

Bouwman, J., de Koter, A., Dominik, C., & Waters, L. B. F. M. 2003, A&A, 401, 577

Bouwman, J., Meeus, G., de Koter, A., et al. 2001, A&A, 375, 950

Bradley, J. P., Humecki, H. J., & Germani, M. S. 1992, ApJ, 394, 643

Brucato, J. R., Colangeli, L., Mennella, V., Palumbo, P., & Bussoletti, E. 1999, *Planetary and Space Science*, 47, 773

Calvet, N., Hartmann, L., & Strom, S. E. 2000, *Protostars and Planets IV*, 377

Carter, B. S. 1990, MNRAS, 242, 1

Chihara, H., Koike, C., Tsuchiyama, A., Tachibana, S., & Sakamoto, D. 2002, A&A, 391, 267

Cohen, M. 1973, MNRAS, 161, 97

Cohen, M., Walker, R. G., Carter, B., et al. 1999, AJ, 117, 1864

Crovisier, J., Leech, K., Bockelée-Morvan, D., et al. 1997, Science, 275, 1904

Cutri, R. M., Skrutskie, M. F., van Dyk, S., et al. 2003, *VizieR Online Data Catalog*, 2246, 0

de Winter, D., van den Ancker, M. E., Maira, A., et al. 2001, A&A, 380, 609

de Winter, D., van den Ancker, M. E., Perez, M. R., et al. 1996, A&AS, 119, 1

Demyk, K., Dartois, E., Wiesemeyer, H., et al. 2000, ISO beyond the peaks: The 2nd ISO workshop on analytical spectroscopy. Eds. A. Salama, M.F.Kessler, K. Leech & B. Schulz. ESA-SP 456., 456, 183

Desch, S. J. & Cuzzi, J. N. 2000, Icarus, 143, 87

Dorschner, J., Begemann, B., Henning, T., Jäger, C., & Mutschke, H. 1995, A&A, 300, 503

Dullemond, C. P. & Dominik, C. 2004, A&A, 417, 159

Dullemond, C. P., Dominik, C., & Natta, A. 2001, ApJ, 560, 957

Eiroa, C., Garzón, F., Alberdi, A., et al. 2001, A&A, 365, 110

Eisner, J. A., Lane, B. F., Akeson, R. L., Hillenbrand, L. A., & Sargent, A. I. 2003, ApJ, 588, 360

Fabian, D., Henning, T., Jäger, C., et al. 2001, A&A, 378, 228

Fabian, D., Jäger, C., Henning, T., Dorschner, J., & Mutschke, H. 2000, A&A, 364, 282

Fouque, P., Le Bertre, T., Epchtein, N., Guglielmo, F., & Kerschbaum, F. 1992, A&AS, 93, 151

Gail, H.-P. 2004, A&A, 413, 571

Glass, I. S. & Penston, M. V. 1974, MNRAS, 167, 237

Glindemann, A., Algomedo, J., Amestica, R., et al. 2003, in Interferometry for Optical Astronomy II. Edited by Wesley A. Traub. Proceedings of the SPIE, Volume 4838, pp. 89-100 (2003), 89–100

Grady, C. A., Polomski, E. F., Henning, T., et al. 2001, AJ, 122, 3396

Grady, C. A., Sitko, M. L., Russell, R. W., et al. 2000, Protostars and Planets IV, 613

Hallenbeck, S. & Nuth, J. 1997, Ap&SS, 255, 427

Harker, D. E. & Desch, S. J. 2002, 565, L109

Herbig, G. H. 1960, ApJS, 4, 337

Hillenbrand, L. A., Strom, S. E., Vrba, F. J., & Keene, J. 1992, ApJ, 397, 613

Honda, M., Kataza, H., Okamoto, Y. K., et al. 2004, ApJ, 610, L49

—. 2003, ApJ, 585, L59

Jäger, C., Molster, F. J., Dorschner, J., et al. 1998, A&A, 339, 904

Joint IRAS Science Working Group. 1988, in IRAS Point Source Catalog (1988)

Kemper, F., Vriend, W. J., & Tielens, A. G. G. M. 2004, ApJ, 609, 826

Lawrence, G., Jones, T. J., & Gehrzi, R. D. 1990, AJ, 99, 1232

Leinert, C., Graser, U., Waters, L. B. F. M., et al. 2003, in Interferometry for Optical Astronomy II. Edited by Wesley A. Traub . Proceedings of the SPIE, Volume 4838, pp. 893-904 (2003), 893–904

MacKinnon, I. D. R. & Rietmeijer, F. J. M. 1987, Reviews of Geophysics, 25, 1527

Malfait, K., Bogaert, E., & Waelkens, C. 1998a, A&A, 331, 211

Malfait, K., Waelkens, C., Waters, L. B. F. M., et al. 1998b, A&A, 332, L25

Mannings, V. & Sargent, A. I. 1997, ApJ, 490, 792

Meeus, G., Bouwman, J., Dominik, C., Waters, L. B. F. M., & de Koter, A. 2002, A&A, 392, 1039

Meeus, G., Sterzik, M., Bouwman, J., & Natta, A. 2003, A&A, 409, L25

Meeus, G., Waters, L. B. F. M., Bouwman, J., et al. 2001, A&A, 365, 476

Mendoza, E. E. 1967, Boletin de los Observatorios Tonantzintla y Tacubaya, 4, 149

Min, M., Hovenier, J. W., & de Koter, A. 2003, A&A, 404, 35

Molster, F. J., Demyk, A., D'Hendecourt, L., & Bradley, J. P. 2003, in Lunar and Planetary Institute Conference Abstracts, 1148–+

Natta, A., Prusti, T., Neri, R., et al. 2001, A&A, 371, 186

Palla, F. & Stahler, S. W. 1993, ApJ, 418, 414

—. 1999, ApJ, 525, 772

Pilipp, W., Hartquist, T. W., Morfill, G. E., & Levy, E. H. 1998, *A&A*, 331, 121

Przygoda, F., van Boekel, R., Àbrahàm, P., et al. 2003, *A&A*, 412, L43

Reimann, H., Weinert, U., & Wagner, S. 1998, in *Proc. SPIE Vol. 3354*, p. 865-876, *Infrared Astronomical Instrumentation*, Albert M. Fowler; Ed., Vol. 3354, 865-876

Rietmeijer, F. J. M. 1989, in *Lunar and Planetary Science Conference*, 513-521

Rietmeijer, F. J. M., Nuth, J. A., & Karner, J. M. 1999, *ApJ*, 527, 395

Rietmeijer, F. J. M., Nuth, J. A., & MacKinnon, I. D. R. 1986, *Icarus*, 66, 211

Servoin, J. L. & Piriou, B. 1973, *Phys. Stat. Sol. (b)*, 55, 677

Siess, L., Dufour, E., & Forestini, M. 2000, *A&A*, 358, 593

Skinner, S. L., Brown, A., & Stewart, R. T. 1993, *ApJS*, 87, 217

Smith, B. A. & Terrile, R. J. 1984, *Science*, 226, 1421

Spitzer, W. G. & Kleinman, D. A. 1960, *Physical Review*, 121, 1324

Strom, K. M., Strom, S. E., Wilkin, F. P., et al. 1990, *ApJ*, 362, 168

Suttner, G. & Yorke, H. W. 2001, *ApJ*, 551, 461

Sylvester, R. J., Skinner, C. J., Barlow, M. J., & Mannings, V. 1996, *MNRAS*, 279, 915

van Boekel, R., Min, M., Leinert, C., et al. 2004a, *Nature*, 432, 479

van Boekel, R., Waters, L. B. F. M., Dominik, C., et al. 2003, *A&A*, 400, L21

—. 2004b, *A&A*, 418, 177

van den Ancker, M. E., Bouwman, J., Wesselius, P. R., et al. 2000, *A&A*, 357, 325

van den Ancker, M. E., de Winter, D., & Tjin A Djie, H. R. E. 1998, *A&A*, 330, 145

Vandenbussche, B., Dominik, C., Min, M., et al. 2004, *A&A*, in press

Vrba, F. J., Strom, S. E., & Strom, K. M. 1976, *AJ*, 81, 317

Waters, L. B. F. M., Cote, J., & Geballe, T. R. 1988, *A&A*, 203, 348

Waters, L. B. F. M. & Waelkens, C. 1998, *ARA&A*, 36, 233